UNIVERSITY OF AMSTERDAM

VU VRIJE UNIVERSITEIT AMSTERDAM

MSc Physics & Astronomy

Advanced Matter and Energy Physics

Master Thesis

Spectrum-Splitting Concepts for Parallel-Stacked Tandem Solar Cells

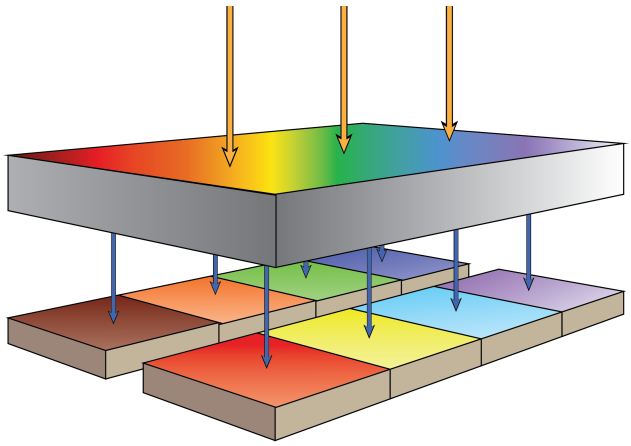

by

Tom Veeken

Student nr.: 10447571

July 2017
60 ECTS
August 2016 - July 2017

1st Examiner:
Prof. Dr. Albert Polman

2nd Examiner:
Prof. Dr. Tom Gregorkiewicz

Supervisor:
Dr. Mark Knight

AMOLF

Master Thesis, University of Amsterdam & VU University Amsterdam, July 2017
Spectrum-Splitting Concepts for Parallel-Stacked Tandem Solar Cells
Tom Veeken

Cover image: A. Polman and H. A. Atwater, *Photonic design principles for ultrahigh-efficiency photovoltaics*, Nature Materials **11**, 174 (2012). [1]

A digital version of this thesis can be downloaded from `http://www.lmpv.nl/theses/`.

The only way to do great work is to love what you do.
If you haven't found it yet, keep looking. Don't settle.

- Steve Jobs

Contents

1

Introduction

1.1 Multi-junction solar cells

Photovoltaics (PV) proved to be both a sustainable and economically-viable energy source by reaching the point of 'socket parity', indicating the generation of electricity by solar panels at the same cost as generated by fossil fueled electricity plants [2]. Reaching socket parity was primarily achieved by lowering the production costs of the complete PV systems, rather than by (drastically) increasing the efficiency of the PV modules or using less material. Although PV efficiency records are continuously broken, the efficiency of single-junction solar cells is always limited by the Shockley-Queisser (S-Q) limit of 33.4% [3]. The S-Q model provides a thermodynamic analysis of the efficiency limit of a solar cell, assuming one electron-hole pair is created per absorbed photon that has an energy of at least the bandgap of the solar cell. So even in the ideal case of the S-Q model for a single-junction, solar energy cannot be harvested with high efficiency.

Polman and Atwater (2012) divided the thermodynamic losses in solar-energy conversion in 6 categories, 3 of which are intrinsic losses [1]. The other 3 categories are single-junction device losses that could potentially be overcome. The first 2 are entropy losses due "to lack of angle restriction" and "incomplete light trapping and reduced QE"; solutions to these losses are "surface light directors" and "light-trapping structures, density of states engineering" respectively [1]. The last category refers to the "energy loss due to thermalization or lack of absorption", which is the main loss mechanism [1]. For instance, for a single-junction silicon solar cell (bandgap: 1.12 eV), this energy loss amounts to ~58% (Figure 1.1).

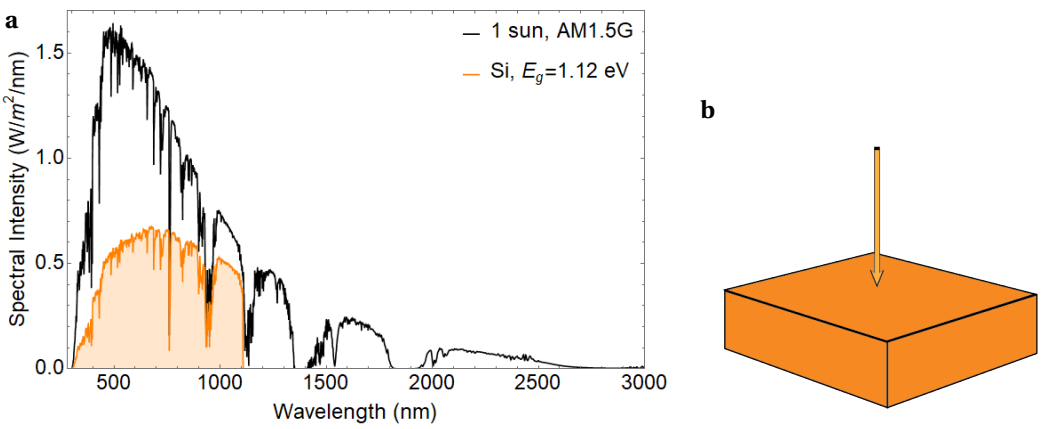

Figure 1.1: *(a) AM1.5G solar irradiation spectrum (black line) and energy utilization spectrum (orange) for an ideal silicon solar cell (bandgap: 1.12 eV, S-Q efficiency limit: 33.4%). (b) Single-junction device schematic corresponding to the spectrum in (a).*

The theoretical S-Q efficiency limit for a single-junction solar cell of 33.4% isn't particularly high, but even world-record solar cells come short a few percent of this theoretical limit. Figure 1.2 shows the efficiencies obtained for all world-record single-junction solar cells of different types and the corresponding S-Q limit, as a function of the bandgap.

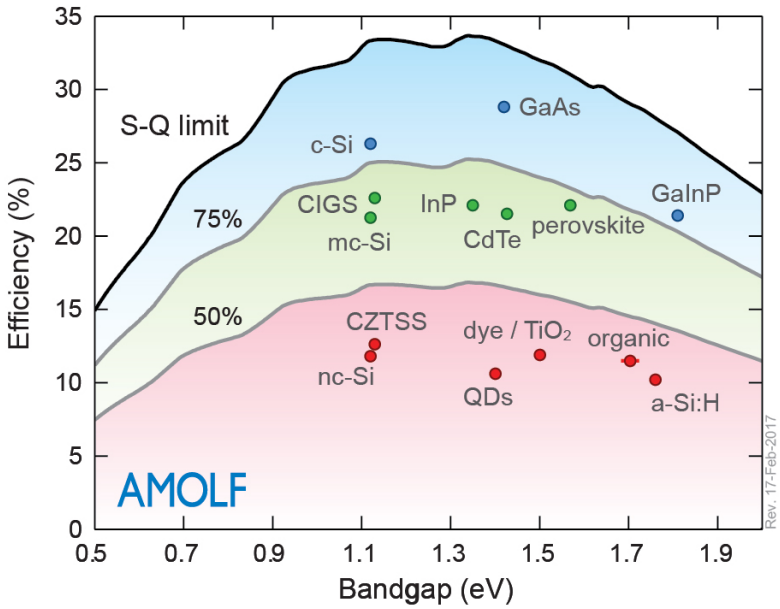

Figure 1.2: *Fraction of the Shockley-Queisser detailed-balance limit (black line) achieved by record-efficiency solar cells, as a function of the bandgap [4]. Gray lines show 75% and 50% of the limit. This figure is continuously updated with data from new record-efficiency solar cells and made available at* `www.lmpv.amolf.nl/SQ/`

Because large size solar panels always perform less than the world-record solar cells due to fabrication imperfections, single-junction solar panels will never reach very high efficiencies. A solution to overcoming the energy losses that are inherent to a single-junction, is the use of a multi-junction solar cell: two or more different solar cells are used together that each convert a portion of the solar spectrum into electricity. This approach ensures that the energy of the short wavelength photons is used efficiently in high bandgap solar cells, while the long wavelength photons are absorbed in lower bandgap solar cells. Because the main energy losses in a single-junction solar cell are due to thermalization and lack of absorption, there is a large potential gain when a multi-junction solar cell is considered.

To form a multi-junction, the subcells can be stacked either vertically or parallel. Until now, most of the fabricated multi-junction solar cells are vertically stacked and series connected. In the following two sections, the vertically and parallel stacked multi-junction solar cells are described to sketch a background of the field.

1.2 Vertically stacked multi-junction solar cells

The conventional approach to the fabrication of a multi-junction solar cell is stacking multiple cells on top of each other, which are ordered by bandgap from high to low (top to bottom). Monolithically integrated tandems (Figure 1.3b shows a 2J version) are interconnected in series within the device, which means that the current through the whole device is the same, while the total voltage output is the sum of the voltages that are generated by the individual cells. Because the generated currents of the subcells must be equal, these types of tandems require current matching and are often referred to as 'constrained tandems'. In this configuration, the individual layers are sequentially deposited on top of each other.

Mechanically stacked tandems (Figure 1.3a shows a 2J version) are composed of two or more individual solar cells that are placed on top of each other, which can then connected in series or in parallel outside the device. They require two electrodes per cell, while all but the bottom electrode must be transparent because the light must be able to reach the bottom cell. In the parallel connected case, the voltage generated by the subcells must be equal and the total current output is the sum of the individual currents. The parallel connected tandem has the advantage over the series connected device that the open circuit voltage (V_{OC}) scales logarithmically with the light intensity, while the short circuit current (I_{SC}) scales linearly. Conversely, the V_{OC} is affected more by temperature changes than the I_{SC}. 'Unconstrained tandems' are electrically independent and yields a higher maximum theoretical efficiency than constraint tandems.

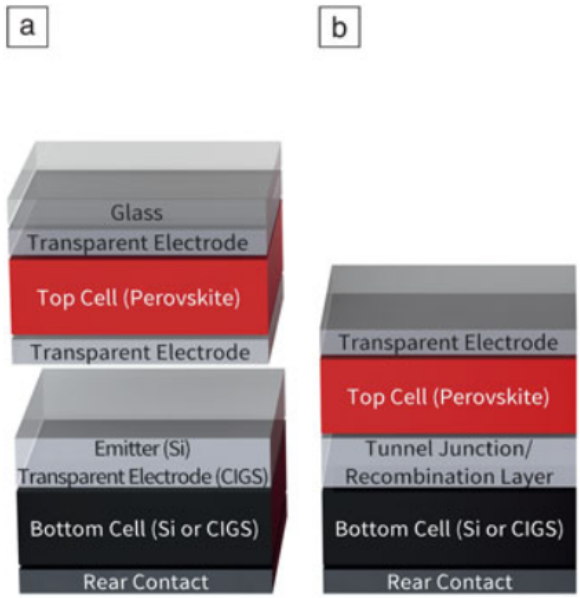

Figure 1.3: *Tandem solar cell architectures. (a) Mechanically stacked tandem; top and bottom cell are individually electrically connected. (b) Monolithically integrated tandem; top and bottom cell are electrically connected in series. (Figure from ref. [5])*

1.2.1 Efficiency limits vs. records

In the ideal case, the first cell, with the highest bandgap, absorbs all the light with an energy that is higher than it's bandgap. The rest of the light, with energy lower than the bandgap of the first cell, is transmitted and reaches the second cell underneath. This cell absorbs all the light that reaches it with an energy higher than it's bandgap and transmits the remaining light. This is continued for each subcell. Figure 1.4a shows the theoretically absorbed light for a three junction (3J) solar cell device, where the colors indicate which portion is absorbed by which subcell (Figure 1.4b).

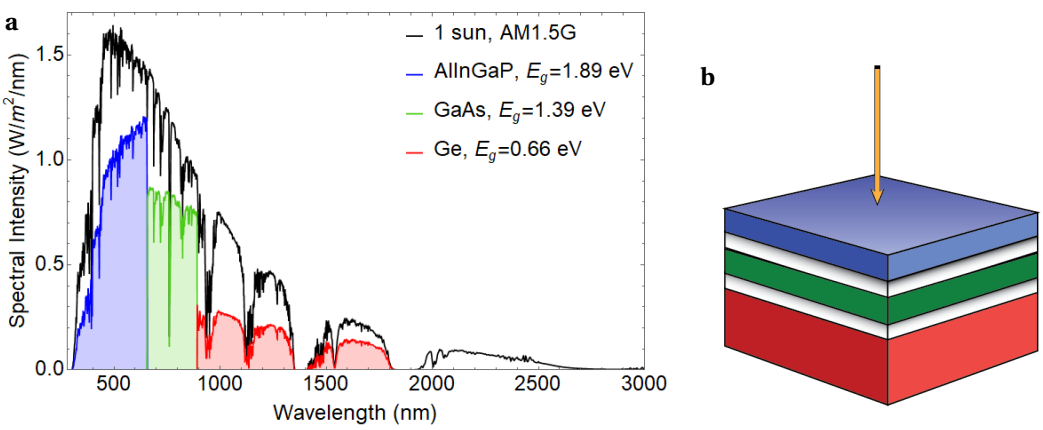

Figure 1.4: *(a) AM1.5G solar irradiation spectrum (black line) and energy utilization spectra (colors) for an ideal multi-junction solar cell (bandgaps: 1.89/1.39/0.66 eV, S-Q efficiency limit: 51%). (b) Multi-junction device design corresponding to the spectra in (a).*

A constrained 3J stack has an efficiency limit of 51.58% under AM1.5G, 1 sun illumination for the ideal bandgap combination (1.90/1.37/0.94 eV), nearly 20% higher than that of a single-junction solar cell (33.68%) [6]. Though, the current world record for a 3J solar cell under AM1.5G, 1 sun illumination is not as high as this limit; 37.9 ± 1.2% efficiency for a three junction cell (1.89/1.39/1.00 eV) [7].

1.2.2 Disadvantages

The above-mentioned record cells perform quite good, considering that their efficiencies reach about 73% of the theoretical limits. But there are also some disadvantages to the use of vertically stacked tandems. Some of these disadvantages are geometry dependent and are therefore set out per geometry below.

One disadvantage that doesn't depend on the geometry but on how the subcells are electrically connected, is a limitation that is called 'current matching'. Current matching is required when the subcells that a tandem is composed of are connected in series; because the current of the device flows through all subcells, this current will equal that of the subcell that generates the lowest current. Therefore the design of a tandem is constraint to the use of subcells with the same or at least similar photocurrent, which is why this type of tandem is called a 'constraint stack'. The generated photocurrent of a subcell in a tandem geometry depends on its bandgap and the bandgaps of the other subcells. Bremner, Levy, and Honsberg showed with a rapid flux calculation method that the optimal bandgap combinations for tandem solar cells differ between unconstrained and constrained stacks, while the theoretical efficiency limit differences are less than 1% (up to 8J tandems, see Figure 1.5) [6]. This implies that different material combinations are wanted for unconstrained tandems than are used for constrained tandems. In addition, the efficiency limit of a constrained tandem is more sensitive to bandgap variations than the efficiency limit of an unconstrained tandem [6]. This is of particular importance regarding the material choice constraints that are set by the need for epitaxial growth of the subsequent layers. It might very well be that the materials that are needed to create the ideal bandgap combination cannot be grown on top of each other. Choice of semiconductor material for the different subcells must thus fulfill both the bandgap combination and lattice constant matching constraints.

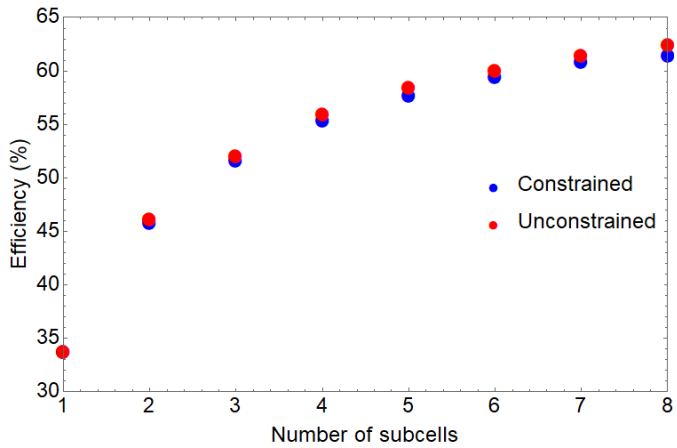

Figure 1.5: *Power conversion efficiency of an ideal stack of solar cells, as a function of the number of solar cells (subcells) in the stack, for a constrained stack (current-matched) and an unconstrained stack (subcells are individually electrically connected). These values were calculated using the AM1.5G solar spectrum, under 1 sun illumination. (Data taken from ref. [6])*

Disadvantages of mechanically stacked tandems

A mechanically stacked 2J tandem (Figure 1.3a) consists of two separate solar cells, that are put on top of each other. For light to reach the bottom cell, all three electrodes above the bottom cell should be transparent. Because all transparent electrodes are not 100% transparent, the middle two electrodes already account for some loss as compared to monolithically integrated tandems. In addition, the need for transparent electrodes imposes constraints on the materials that can be used, which might result in some material related problems. For instance, when the top cell is a perovskite, ITO or silver nanowires are options as transparent electrodes [5]. But problems arise when these electrodes are to

be deposited onto the perovskite cell. For the ITO, sputter deposition might damage the perovskite layer, as well as annealing after deposition, which is desired to enhance its performance [5]. For silver nanowires, the lateral conductivity of the perovskite's window layers might be insufficient, and the formation of insulating halide complexes may compromise performance [5].

In addition to transparency and fabrication related issues of the electrode layers, parasitic absorption ("absorption in the solar cell that does not contribute to photocurrent" [5]) by those and any other layers in the device can be an issue.

Disadvantages of monolithically integrated tandems

A monolithically integrated 2J tandem (Figure 1.3a) consists of two solar cells that are fabricated on top of each other and are inherently series connected. Such multi-junction solar cells are generally fabricated layer by layer by metalorganic chemical vapor deposition (MOCVD) [8]. It requires lattice matching of the individual layers to epitaxially grow homogeneous, stable and flat layers on top of each other, which constraints the choice of material in addition to the current-matching material constraints. In addition, tunnel barrier layers are needed in between each two subcells, causing little but nonzero parasitic absorption.

Another disadvantage of monolithic tandems is their poor durability. Depositing solar cells on top of each other through solution processing may yield good performance but poor stability, as reported by Moon et al. in 2015 for their DSSC/CIGS monolithic tandem [9].

1.3 Parallel stacked multi-junction solar cells

Instead of vertically stacking solar cells on top of each other, one could think of a parallel stacked multi-junction solar cell. Such a design inherently doesn't have the problems associated with a vertical design, such as current-matching (cells are individually electrically connected), the need for transparent electrodes and epitaxial growth constraints of subsequent layers. Such a parallel-stacked tandem solar cell should look something like the design depicted in Figure 1.6. In this architecture, the solar spectrum impinges onto a (photonic) spectrum splitting layer. This layer splits the sunlight into eight distinct spectral bands and subsequently directs each band to the subcell that is optimized for the corresponding spectral band and concentration factor. In this fashion, carrier thermalization

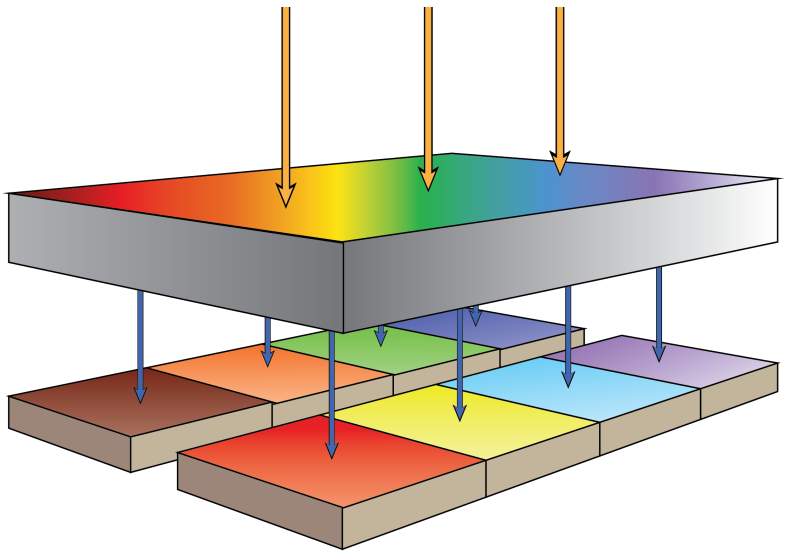

Figure 1.6: *Parallel-stacked tandem solar cell architecture, consisting of 8 individual solar cells (colored tiles) and a spectrum-splitting layer (multi-colored tile) that directs distinct spectral bands of the solar spectrum onto the solar cell, matching the photon energy with the bandgap of the solar cell. (Figure from ref. [1]).*

can be minimized to approximately 10% [1] and one has full flexibility regarding semiconductor material choice for the different subcells (as opposed to the vertically stacked tandem). Such a design should then be able to get closer to the efficiency limit for unconstrained 8J tandems of 62.34% [6] than current multi-junction solar cells do.

Polman and Atwater write that the design of Figure 1.6 is a "Parallel- connected architecture that can be realized using epitaxial liftoff and printing techniques of the semiconductor layers, followed by printing of a micro- or nanophotonic spectrum splitting layer" [1]. Assuming that the challenge of printing multiple different solar cells in a pixelated array is indeed possible, one needs to design a spectrum-splitting layer that reroutes the solar spectrum to the right subcell. The goal of this work is to investigate different candidates for such a spectrum-splitter. After literature review of different approaches to light rerouting and spectrum-splitting, three candidates were chosen. Therefore, this thesis is divided into three projects that are each described in an individual chapter.

First, in Chapter 2, we describe the work we performed to investigate the behavior of multiple V-shaped nanoantennas placed close to each other, that individually exhibit bidirectional scattering of visible light. We show that placing two antennas in each other's vicinity enhances the relative bidirectional scattering efficiency, which suggests that using many of these antennas in a grid might function as a spectrum-splitting metasurface.

Subsequently, in Chapter 3, we investigate the use of an inverse design algorithm that was used to design unintuitive structures with wavelength demultiplexing properties for infrared light. We report for the first time that the initial material parameters influence the final optimized design and that the use of transparent materials (for visible light) limits the efficiency of the optimized design, but increases its robustness against manufacturability constraints.

Finally, we present our work on a spectrum-splitting tapered waveguide in Chapter 4 (theory and simulations) and Chapter 5 (fabrication and characterization). Because this approach was perceived by us as the best approach to the envisioned spectrum-splitting layer (compared to the other projects), we chose to start fabrication of the tapered waveguide after we obtained a proof of concept by means of FDTD simulations. Besides the theory and simulations of the spectrum-splitting capabilities of the taper, we show the characterization of the fabricated structures. Finally, we discuss a first experimental demonstration trial of the spectrum-splitting effect, and designs for new experimental setups to achieve successful demonstration in the future.

2

Enhanced bidirectional scattering by two V-shaped nanoantennas

Bidirectional scattering by a resonant V-shaped nanoantenna has been shown by Li et al. [10], causing visible light of different wavelengths to be scattered into diametrically opposite directions at the scale of the antenna. Based on this phenomenon, we envisioned a metasurface composed of many V-shaped antennas that causes the same bidirectional scattering effect on a larger scale, thereby effectively acting as a spectrum-splitting layer. To investigate the feasibility of such a metasurface, we first reproduced the bidirectional scattering by individual V-shaped antennas in FDTD simulations. Normalizing the extinction of the incident light by the geometrical cross section of the V-shaped antenna, we quantify that the extinction is over 8 times larger than the geometrical cross section around a wavelength of 700 nm. Subsequently, we determined that the V-shaped antennas keep exhibiting bidirectional scattering when placed next to each other. Moreover, the bidirectional scattering efficiency is ~1.5 times higher when two V-shaped antennas are placed very close together, relative to a single antenna. Although this result indicates that a V-shaped antenna could be used as the building block of a spectrum-splitting metasurface, the bidirectional scattering is achieved for a narrow spectral band. Future work should point out whether it's possible to create a broadband spectrum-splitting metasurface that is composed of narrow-band bidirectional scattering antennas.

2.1 Resonant nanoparticles

Optical antennas have shown extraordinary light manipulation at the nanoscale, such as directional scattering [11, 12], zero backscattering [13], and directional enhanced emission [14]. Such optical antennas have sizes in the order of a visible wavelength (hundreds of nanometers), and therefore interact very differently with incident light than their bulk counterparts. The interaction between a bulk material and light is a combination of reflection, refraction, and absorption of the light by the material. The relative strengths of these interactions are determined by the complex dielectric permittivity of the material $\epsilon_r(\lambda)$, the permittivity of the surrounding medium, the interface between the material and the surrounding medium, and the wavelength of the incident light λ. In contrast, while also being dependent on the relevant parameters for bulk materials, the interaction of an optical antenna with light is strongly dependent on its geometry. Because of the physical size of an optical antenna and the dipolar nature of the electromagnetic field of the light, light can resonate in the vicinity of the nanoscale antenna. Gustav Mie was the first to give a description of such optical resonances by solving Maxwell's equations for plane wave illumination of a gold nano-sphere [15]. Mie theory, as it was later called, although initially written to solve for resonances in metals, holds for both metallic and dielectric nanoparticles. Particularly dielectric nanoparticles with high permittivities strongly enhance the light-matter interaction, causing resonant light scattering called Mie scattering, which significantly increases the scattering cross section compared to the geometrical cross section.

Metasurfaces consisting of resonant nanoparticles can manipulate an incident wave front, altering its shape by the resonant interaction with individual and/or a collection of nanoparticles, giving rise to phenomena that are not found in non-resonant systems, such as optical vortices [16], dispersive holography [17], and anomalous reflection and refraction [16, 18]. Such a metasurface can only be designed for a specific purpose if the resonances of the building blocks, the nanoparticles, are understood. So, for the purpose of spectrum-splitting, one might think of a metasurface that splits an incident spectrum into at least two parts, redirecting each in a different direction. Spectrum-splitting for photovoltaics naturally limits us to the solar spectrum, for which we want to design a metasurface that splits it into two broad spectral-bands, moving in opposite direction. The building block of such a metasurface should thus be a wavelength-dependent scatterer, with minimal absorption losses. A good candidate for such a scatterer would be a dielectric nanoparticle because of the low optical losses in the visible and near-infrared, which make up the larger portion of the solar spectrum. And it would have to be asymmetrically shaped, in order for the different resonant modes (Mie modes) to spatially interfere differently for different wavelengths. Li et al. (2016) showed that their silicon V-shaped antennas exhibit bidirectional scattering for visible wavelengths due to their asymmetrical shape and relatively low absorption cross section [10], making these V-shaped antennas interesting building blocks for a spectrum-splitting metasurface.

In the following section, the resonant behavior of the V-shaped antennas is described based on the work of Li et al. [10]. Then the FDTD simulations are discussed that we performed analogous to the simulations of Li et al., to characterize and quantify the extinction of single antennas. Finally, the interplay between two V-shaped antennas is analyzed as a function of the distance between them, were we show that V-shaped antennas placed very close together show enhanced relative bidirectional scattering, suggesting that many of these antennas together could create a spectrum-splitting metasurface.

2.2 Bidirectional scattering by V-shaped nanoantennas

Single silicon V-shaped antennas have shown bidirectional scattering for visible wavelengths, scattering red and green light in diametrically opposite directions [10]. Figure 2.1 shows the concept, as well as the scattering patterns and a SEM image of a V-shaped antenna as fabricated by Li et al. [10]. Both simulation and experimental results showed bidirectional scattering for wavelengths $\lambda_1 \approx 755$ nm and $\lambda_2 \approx 660$ nm, for which the simulated scattering patterns are shown. The V-shaped antenna was fabricated by plasma enhanced chemical vapor deposition (PECVD) of an amorphous silicon

film on a glass substrate. Subsequent e-beam lithography patterning and inductively coupled plasma (ICP) etching resulted in the desired V-shaped antenna design (see SEM image in Figure 2.1). Using this method, the initial film thickness determines the antenna height (H) and the e-beam lithography pattern determines the other geometrical parameters: the width (W), length (L) and opening angle (α) of the antenna (see schematic in Figure 2.1).

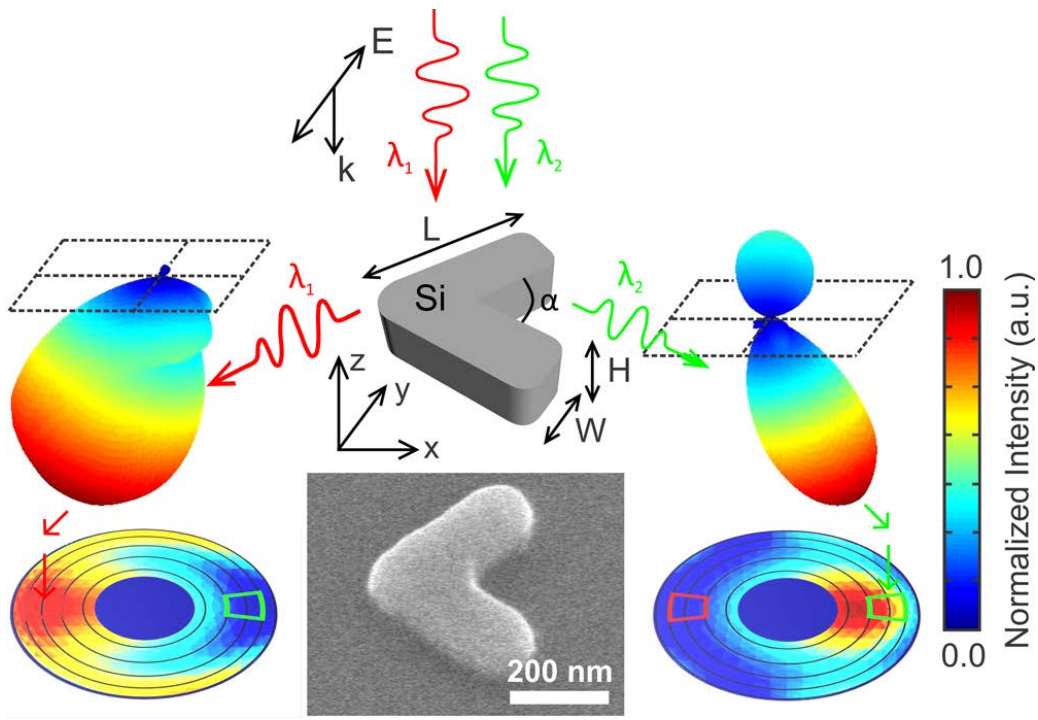

Figure 2.1: *Bidirectional scattering by a V-shaped antenna. (Middle) schematic representation of the rerouting of red ($\lambda_1 \approx 755$ nm) and green ($\lambda_2 \approx 660$ nm) light into diametrically opposite directions. (Sides) 3D scattering patterns and corresponding 2D projections as calculated using FDTD simulations, showing the bidirectional scattering effect. Red and green boxes in the 2D projections are used to calculate the directivity, as shown in Figure 2.2. (Bottom) SEM image of the fabricated V-shaped antenna, which is used to determine the geometrical parameters of the antenna. (Figure from ref. [10])*

Ellipsometry data of the deposited amorphous silicon film and the geometrical parameters as determined by scanning electron microscopy (SEM) were used to accurately model the antenna in FDTD simulations. The bidirectional scattering has been quantified by simulating and measuring the extinction and the directivity spectra of the antenna, which are shown in Figure 2.2. The extinction is defined as the sum of the absorption and scattering of the V-shaped antenna. In FDTD simulations, the extinction was directly calculated from the absorption and scattering, using the total-field scattered-field method in Lumerical FDTD Solutions to isolate the scattered and absorbed light from the incident light. Experimentally, the extinction spectroscopy was performed using a Fourier transform infrared (FTIR) microscope, while the directivity was determined by measuring the angular scattering profile using a back focal plane (BFP) imaging setup. In simulations, the directivity was calculated from the angular scattering profile on a large monitor box. Comparing the simulated and experimental spectra in panels a and b of Figure 2.2, Li et al. find good agreement between the extinction spectra shape and very good quantitative agreement between the directivity spectra. Panel d shows the experimental angular scattering profiles for the wavelengths indicated by the colored dots in panel c. Also, the red and green boxes indicate the areas that were used to calculate the directivity. Comparing panel d to the simulated angular scattering profiles shown in Figure 2.1, less agreement is found, although bidirectional scattering is still profound. Note that both in simulation and experiment the bidirectional scattering occurs on the flanks of the strong extinction resonance around 695 nm.

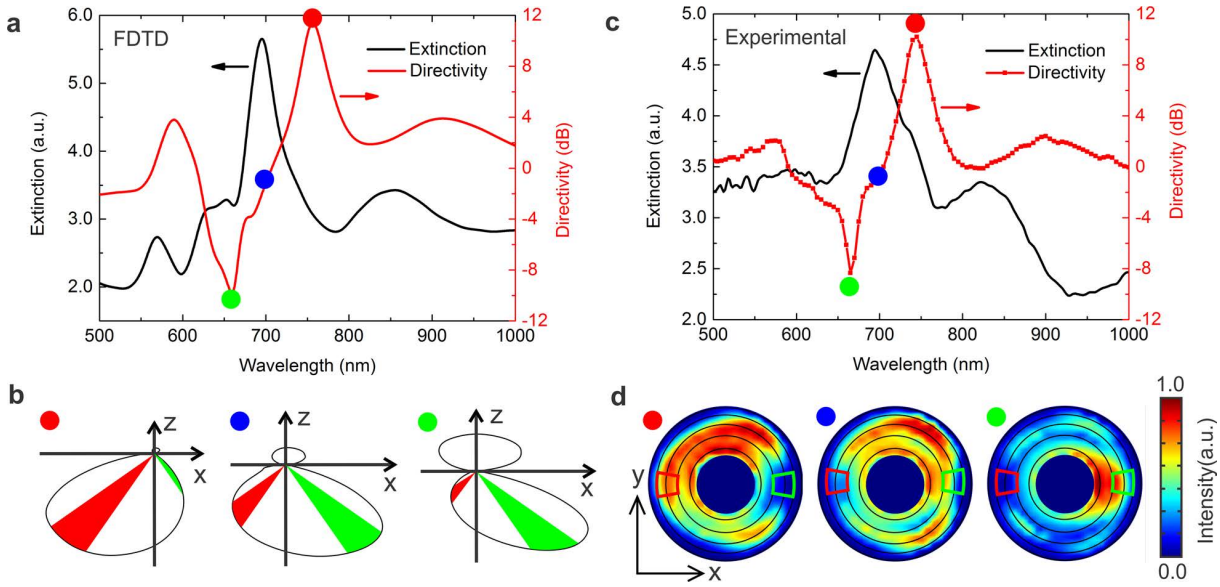

Figure 2.2: *FDTD and experimental results for the Si antenna on a glass substrate, as shown in Figure 2.1. (a) Extinction and directivity spectra calculated by FDTD simulations. (b) Sketched scattering profiles in the xz-plane for the wavelengths indicated by the colored dots in panel (a). (c) Experimental extinction and directivity spectra for a V-shaped antenna with the same geometry as simulated for panel (a). BFP images of light scattered by the V-shaped antenna, at wavelengths indicated by the colored dots in panel (c). Red and green boxes are used to calculate the directivity shown in panel (c). (Figure from ref. [10])*

The observed bidirectional scattering seems to be a property of a V-shaped antenna as confirmed by simulations and experiments, but must be understood as the collective behavior of a multitude of resonant modes that are present in the antenna. It is critical to understand the individual resonant modes and the interplay between them, in order to design a V-shaped antenna with the desired characteristics. The multipole decomposition that Li et al. performed shows that the bidirectional scattering of a V-shaped antenna can be explained by considering the electric dipole polarized in the y-axis (ED_y), the magnetic dipole polarized in the z-axis (MD_z) and the electric quadrupole oriented in the xy-plane (EQ_{xy}), as shown in Figure 2.3. The directivity of the sum of these three resonances shows good agreement with the observed scattering in the undecomposed FDTD simulation. Note that this multipole decomposition is based on y-polarized plane-wave illumination of a V-shaped antenna in vacuum, which is considered to give valid results for the system on a substrate because the electromagnetic fields are mostly localized inside the antenna. From Figure 2.3b we find that the V-shaped antenna exhibits a particularly strong magnetic dipole, being the main cause for the positively scattered red light at 755 nm. The combination of the electric dipole and quadrupole cause the negatively scattered green light around 660 nm. Now that we can explain the bidirectional scattering of a V-shaped antenna, we can take a look at the extinction and directivity of V-shaped antennas with slightly different geometrical parameters. Because the resonant modes of the antenna depend heavily on the geometry of system, we expect that the resulting extinction and directivity will also change.

In their paper, Li et al. showed that their FDTD simulations of the scattering spectra match their experimentally measured bidirectional scattering [10]. This renders the simulation a tool to predict the bidirectional scattering behavior of a single V-shaped antenna with specific geometrical parameters and of an ensemble of V-shaped antennas. The latter has not been discussed by Li et al., but the former has been done for a range of geometrical parameters, for which the extinction and directivity spectra are available in the Supporting Information of their paper [10, SI]. Figure 2.4 gives an overview of these results, showing that the extinction and directivity of the antenna depend on all four geometrical parameters. Moreover, tuning H and W seems to affect most at which wavelengths

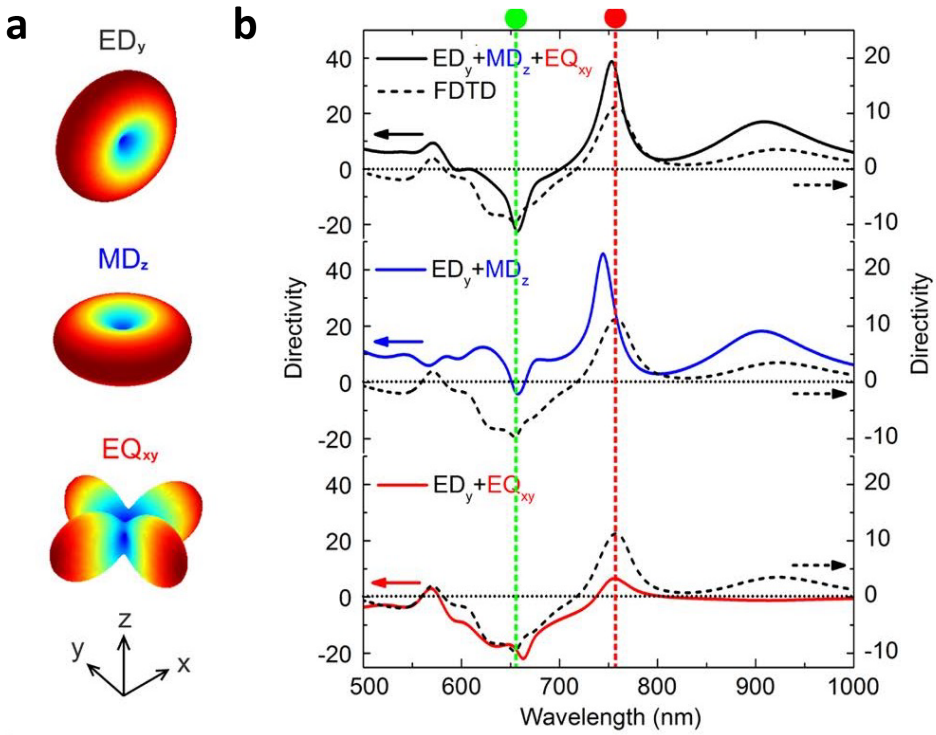

Figure 2.3: *Reconstruction of the bidirectional scattering by multipole decomposition, considering only the ED_y, MD_z, and EQ_{xy} multipoles. (a) Schematical representation of the scattering patterns of the considered multipoles. (b) Directivity spectra as calculated from the sum of the considered multipoles (left axis, solid lines), compared to the directivity as calculated from FDTD simulations (right axis, dashed lines). Green and red lines indicate the directivity extrema that cause the bidirectional scattering behavior. (Figure from ref. [10])*

bidirectional scattering is observed in the simulation results. For the performed parameter sweep, bidirectional scattering occurs through a large part of the visible spectrum, which corresponds with the relevant spectrum when a tandem of GaAs and Si is considered. Extending this parameters sweep has to reveal whether V-shaped antennas can span the full solar spectrum, up until the bandgap of Si around 1100 nm.

Comparison of the spectra in Figure 2.4 reveals that bidirectional scattering always occurs on the flanks of the extinction resonance and scales with the resonance amplitude, rendering the extinction resonance a measure of the bidirectional scattering behavior of the antenna. This observation will be used in the following sections, where we will first calculate the extinction as a measure of bidirectional scattering. After a discussion of the employed FDTD simulation method in section 2.3, we will then analyze the coupling of two V-shaped antennas in section 2.4, to investigate if the bidirectional scattering behavior observed for single V-shaped antennas is preserved when two antennas are placed in each other's vicinity.

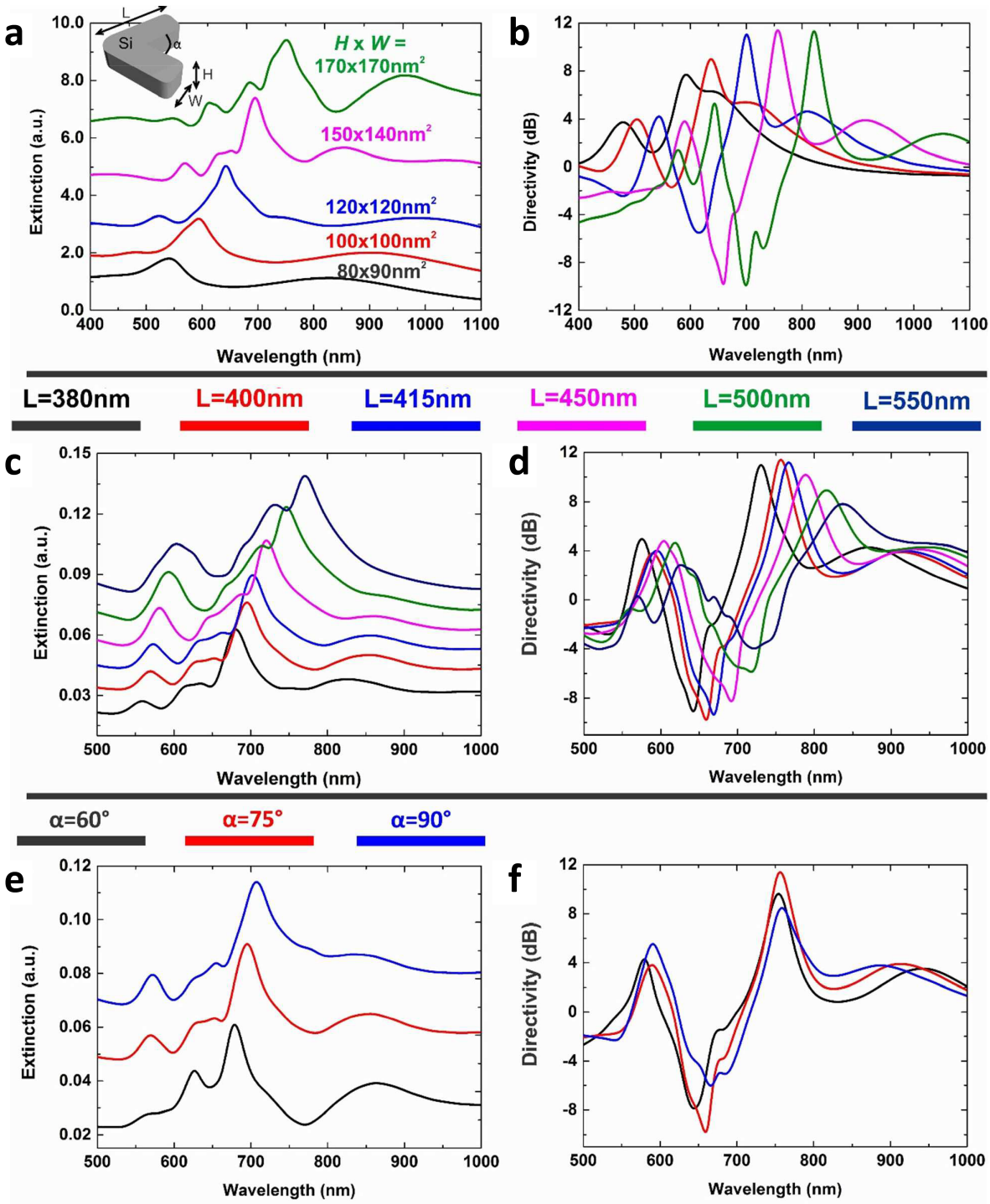

Figure 2.4: *Simulated extinction and directivity curves for all V-shaped antenna geometries reported by Li et al. (a) Extinction and (b) directivity spectra of V-shaped antennas for varying H (height) × W (width), keeping L = 400 nm and α = 75° constant. (c) Extinction and (d) directivity spectra for varying arm length L, keeping H × W = 150 × 140 nm and α = 75° constant. (e) Extinction and (f) directivity spectra for varying opening angle α, keeping H × W = 150 × 140 nm and L = 400 nm constant. Extinction spectra are offset for clarity. (Figures from ref. [10])*

2.3 Finite-difference time-domain simulations

The FDTD simulations on V-shaped antennas that were performed as part of this thesis are all based on the work by Li et al., and thus, to model our simulations as close as possible to theirs, we used the same software, simulation objects and refractive index values. The FDTD simulations were performed in 3 dimensions using Lumerical FDTD Solutions solver v8.15.697. The V-shaped antennas were modeled with rounded corners (see inset in Figure 2.6a), similar as shown in the cartoon by Li et al. (Figure 2.1). By employing a total-field scattered-field (TFSF) source, we separated the scattered field from the transmitted and reflected fields (see Figure 2.5). By measuring the light outside the TFSF source box with a cross section analysis box, we obtained only the scattered light; by placing a cross section analysis box inside the TFSF box, we measured the difference between the incoming and outgoing light, which corresponds to the absorption cross section. The V-shaped antenna was placed on a glass substrate, which was modeled as a lossless dielectric material ($n = 1.52$).

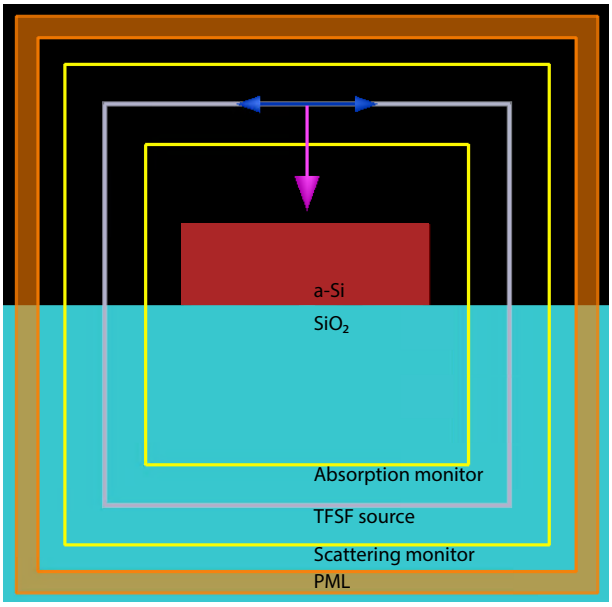

Figure 2.5: *YZ cross-cut of the 3D FDTD simulation in Lumerical. The V-shaped antenna (red square) is placed on top of a glass substrate (blue), which extends through the perfectly matched layers (orange box). A total-field scattered-field (TFSF) source (white box) injects a plane wave with k-vector pointed downwards (purple arrow) and polarized in plane (blue arrows). A scattering cross section monitor (outer yellow box) is placed just outside the TFSF source box, which only transmits scattered fields. An absorption cross section monitor (inner yellow box) is placed close to the antenna, which determines the absorption by calculating the difference between the incoming and outgoing light over its surface.*

2.3.1 Convergence testing

Validation of simulation results is of crucial importance. Besides choosing the appropriate simulation settings and objects, one should check that the simulation accurately meshes with respect to the object dimensions and simulated wavelengths. Figure 2.6a shows the normalized extinction for different simulation mesh sizes. Decreasing the mesh size in all dimensions from 60 to 1 nm, the extinction curve converges, showing very little difference between the curves for 5, 2 and 1 nm mesh size. This proves that the simulated objects are equally well modeled in cubes of 5 or 1 nm, and that there are no simulation artifacts (e.g. infinitely sharp features such as the corners of a cube). Therefore, in order to minimize computation time, we choose a 5 nm mesh size for all subsequent simulations.

The extinction curves shown in Figure 2.6a correspond to a V-shaped antenna with geometrical parameters: H = 150 nm, W = 140 nm, L = 400 nm, and $\alpha = 75°$ (see inset). Comparison of our simulated extinction with the extinction as published by Li et al. [10] (same geometrical parameters) is shown in Figure 2.6b, which shows very good agreement of both resonance wavelengths and relative resonance amplitudes. Note that our simulations show that the extinction is over 8 times larger than the geometrical cross section around 700 nm. Because all extinction spectra were given in arbitrary units in ref. [10], we report this result for the first time.

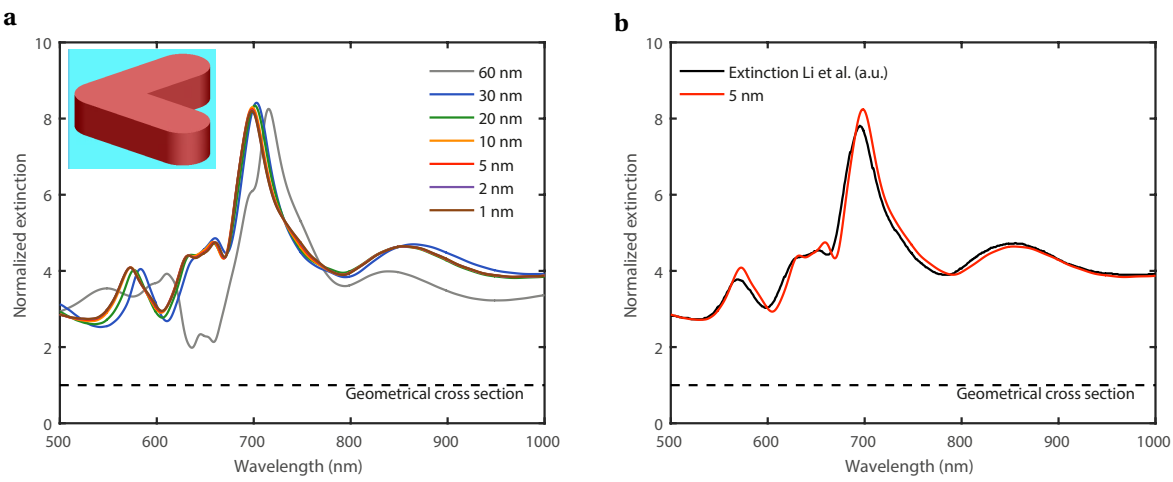

Figure 2.6: *(a) Convergence test of simulation mesh size, indicated for each curve in the legend, of a V-shaped antenna (inset; geometrical parameters: $H = 150$ nm, $W = 140$ nm, $L = 400$ nm, and $\alpha = 75°$). Decreasing the mesh size from 60 to 1 nm, the extinction curve converges, showing very little difference between the curves for 5, 2 and 1 nm mesh size. Therefore we choose a 5 nm mesh size in all subsequent simulations. (b) Comparison of our simulated extinction at 5 nm mesh size, as shown in panel (a), to simulated extinction as published by Li et al. [10]. Our extinction spectrum is normalized to the geometrical cross section of the antenna and shows the same shape as the extinction spectrum from ref. [10], which is reported in arbitrary units.*

2.4 Combining two V-shaped antennas

Being able to successfully simulate the extinction of a single V-shaped antenna, we can now take the next step towards a spectrum-splitting metasurface: simulating the behavior of two antennas next to each other. Figure 2.7 shows the simulated extinction for two V-shaped antennas pointing leftwards (see inset), for pitches ranging from 300 to 2000 nm. The extinction is normalized to the geometrical cross section of two V-shaped antennas, and can, therefore, be compared to the extinction profile of a single antenna, which is also plotted in Figure 2.7. For their extinction spectroscopy measurements, Li et al. fabricated their V-shaped antennas with a pitch of 2000 nm [10]. For this pitch, the normalized extinction is exactly the same as for a single antenna, proving there is no interaction between two antennas at least 2000 nm apart. Reducing the pitch to 600 nm, the spectrum doesn't change, except for the relative amplitudes of the resonances. For pitches of 300 and 400 nm, the main resonance around 700 nm blue shifts, indicating interaction. However, the spectrum is not heavily modified compared to the spectrum of a single V-shaped antenna, suggesting the antennas don't influence each other much.

To check if the collective behavior of two antennas next to each other is spectrum splitting the incident spectrum similar as a single antenna, we calculate the scattered light in a simulation 3 μm below the two antennas. Figure 2.8d shows the light scattered by a single V-shaped antenna (dashed lines) and two antennas with a pitch of 300 nm (solid lines) for the designed bidirectional scattering wavelengths (660 and 755 nm), and a reference wavelength (500 nm). The power spectra are normalized to the amount of V-shaped antennas, showing that the two antennas next to each other scatter ~1.5 times more light relative to a single antenna. Also, the bidirectional scattering is relatively more profound for the two antennas, showing that the bidirectional scattering is enhanced by placing two antennas near each other. The possibility of placing antennas very close to each other without disturbing the resonance effects, but rather increasing the bidirectional scattering efficiency opens up new possibilities for tailoring metasurfaces that spectrally split an incident spectrum.

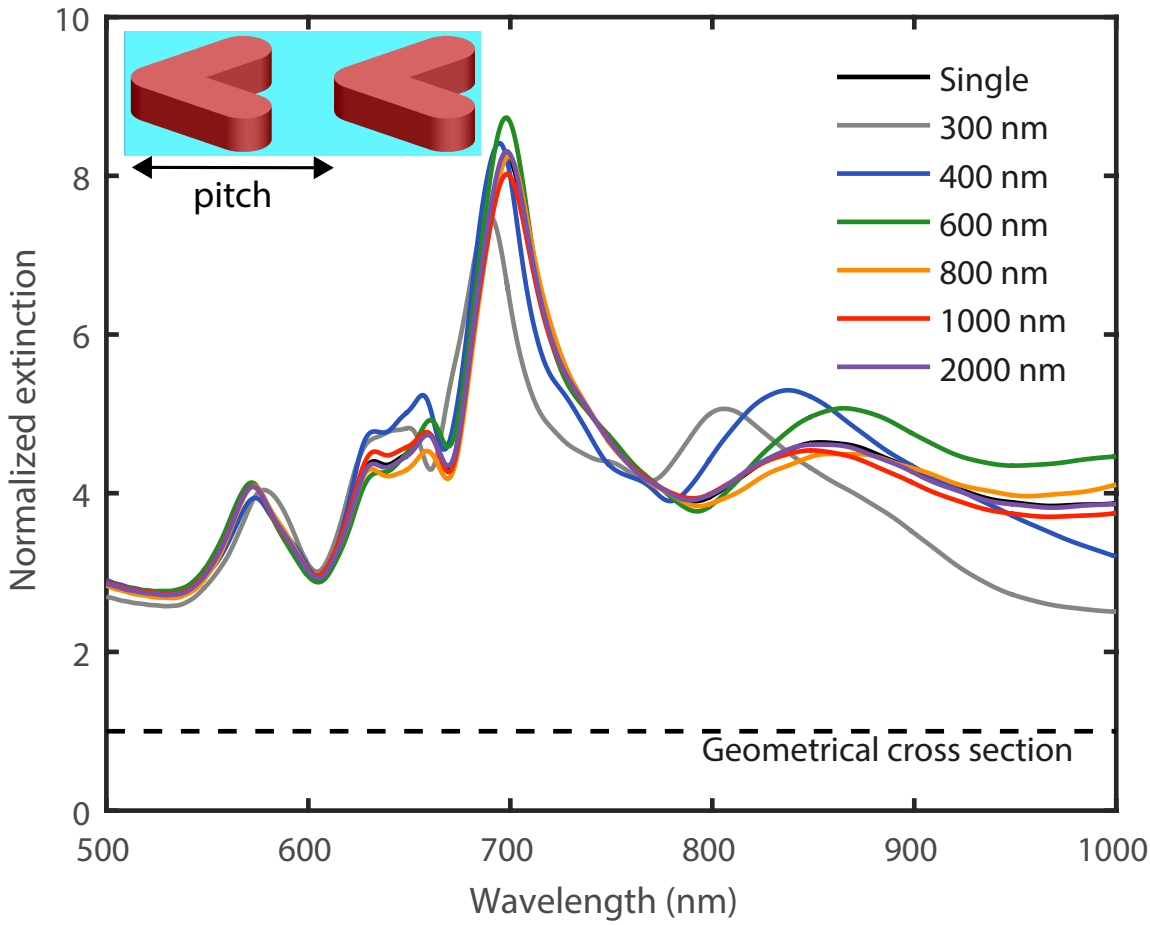

Figure 2.7: *Normalized extinction spectra of two V-shaped antennas placed next to each other (see inset for orientation), compared to the extinction of a single antenna (geometrical parameters of all antennas: $H = 150$ nm, $W = 140$ nm, $L = 400$ nm, and $\alpha = 75°$). Decreasing the pitch size from 2000 to 300 nm, the extinction spectrum blue shifts slightly for small pitches, but the overall shape remains the same, suggesting the antennas don't influence each others behavior much.*

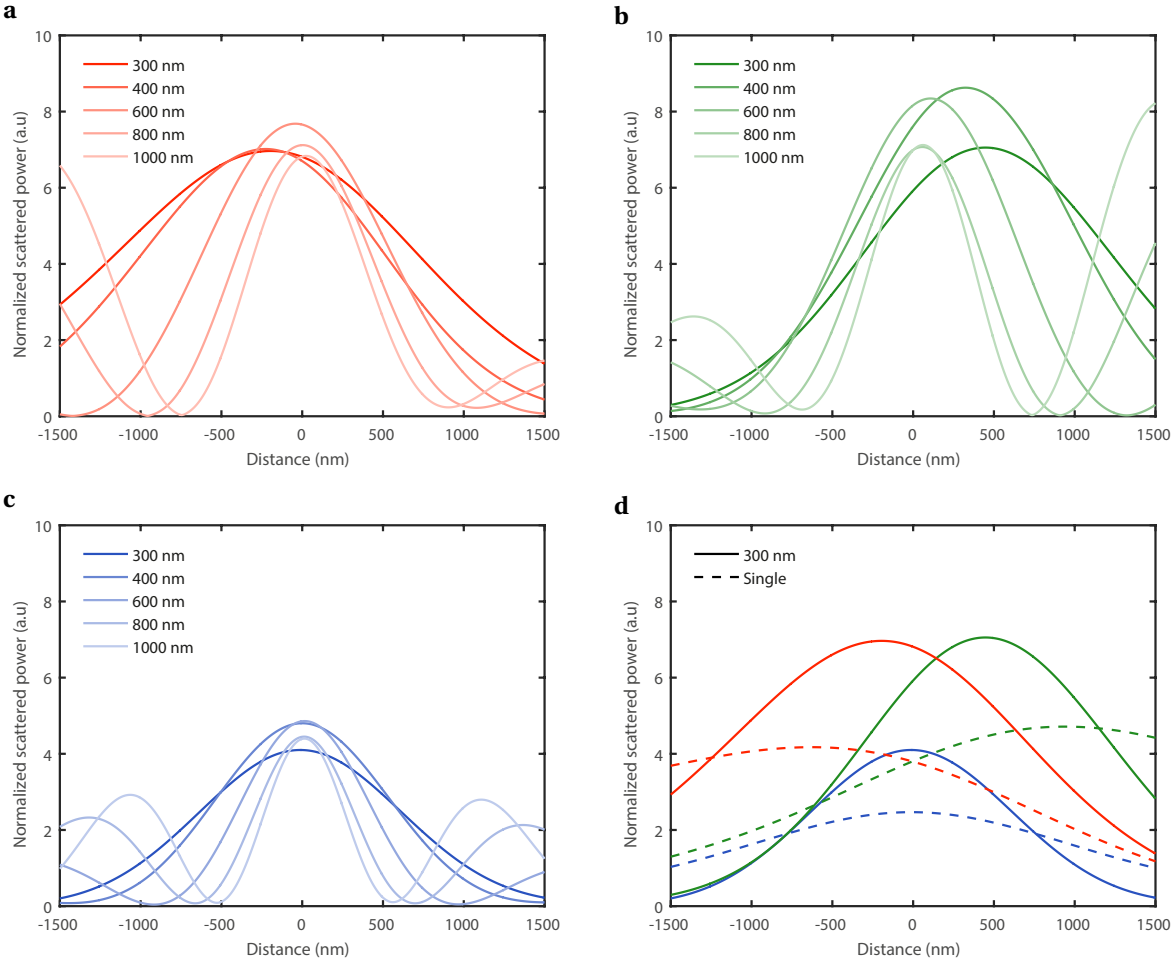

Figure 2.8: *(a,b,c) Scattered power spectra for the antenna configurations considered in Figure 2.7 at a distance of* 3 *µm below the antennas, for wavelengths of* 755 *nm (a),* 660 *nm (b) and* 500 *nm (c). Antennas placed close together show bidirectional scattering for the design wavelengths of* 755 *and* 660 *nm, while blue light is scattered straight down. At large pitches, the two antennas cancel each other's bidirectional scattering effect. (d) Scattered power spectra for a single V-shaped antenna (dashed lines) and two antennas with a pitch of* 300 *nm (solid lines), normalized to the amount of V-shaped antennas. The two antennas placed close together scatter* ~1.5 *times more light relative to the single antenna, and in addition, the bidirectional scattering is more profound, showing that multiple antennas have a more efficient bidirectional scattering effect.*

2.5 Conclusion and outlook

Starting from the V-shaped antenna design by Li et al. [10], we have shown that such antennas can be placed very close together without disturbing their individual bidirectional scattering behavior. Moreover, their scattering efficiency is ~1.5 times higher when placed very close together relative to a single V-shaped antenna, and the bidirectional scattering effect is more profound.

This work shows that V-shaped antennas are suitable candidates as a building block of a spectrum-splitting metasurface. Challenges that remain are the elimination of the absorption in the silicon antenna, for instance by switching to a non-absorptive, high-index material like SiN_3 or TiO_2. Furthermore, for application in a spectrum-splitting photovoltaic system, the spectrum should be split in at least two broad spectral-bands. This could possibly be achieved by combining V-shaped antennas of different shapes and sizes in a metasurface that collectively splits the solar

spectrum in a broadband fashion, despite being composed of many narrow-band spectrum-splitters. Finally, integration of a spectrum-splitting metasurface in a photovoltaic system implicates that it be encapsulated by a medium other than air. Thus the resonant behavior of an encapsulated V-shaped antenna should be considered in advanced integrated spectrum-splitting metasurface designs.

Due to the investigative nature of this master project, the above-mentioned ideas for future work on a spectrum-splitting metasurface based on V-shaped antennas have not been pursued. Instead, we decided to also investigate the other two approaches considered in Chapter 1, to find the best approach among these three.

3

Inverse design of visible light manipulation structures

Optimization algorithms are a powerful means to explore the complete parameter space that is associated with a certain problem. This work was inspired by the work of Piggott et al. [19] about their inverse design algorithm that optimizes for a silicon wavelength demultiplexer that routes two individual wavelengths from a single input waveguide to two different output waveguides. We investigated the possibility of employing this algorithm to design a structure that efficiently splits the solar spectrum into several distinct spectral bands. We found that the initial electric permittivity defined in the optimization algorithm affects the final optimized design, which has not been reported so far. In addition, we found that by changing the material model from silicon to silicon nitride (SiN_3), which is nearly transparent throughout the solar spectrum (as opposed to silicon), the algorithm achieved lower efficiency for the waveguide mode conversion problem that was considered (keeping all other parameters the same). However, the optimized SiN_3 structure proved more robust to the discretization step that is needed to obtain a manufacturable design. This robustness may be an advantage of the SiN_3 design, if near-unity, input to output, conversion efficiencies can be obtained (which has been achieved for the silicon case), by, for example, changing the optimization problem and/or input parameters. If this can be shown in future work, this paves the way for inverse designed, high-efficiency, SiN_3 visible light manipulation structures such as a spectrum-splitter.

3.1 Inverse design algorithm

Metasurfaces based on nanostructures allow the manipulation of light at a subwavelength scale, providing a means to efficient light management in photovoltaics [1, 20]. Such metasurfaces are critical to the performance of any solar cell because they constitute essential parts of an efficient solar cell, such as anti-reflection coatings [21], light-trapping schemes for thin film solar cells [22, 23], and more recently, wavelength selective reflection schemes for colorful solar cells [24].

However, all of these nanophotonic metasurfaces are effectively designed by hand: the designer typically selects a small parameter space over which a brute-force parameter sweep is done in FDTD simulations to find the best performing metasurface configuration. This approach, although proven successful, is inherently inefficient because the search for performance is undirected. This means that the user-chosen parameter space is evaluated in its entirety, which is computationally intensive. In contrast, a directed search for performance by, for example, particle swarm optimization, does not evaluate the chosen parameter space in its entirety [25]. Instead, it iteratively selects a part of the parameter space that is to be evaluated next, based on the steepest increase in (user-defined) performance shown by the parameter space that was evaluated before. Such a directed search can dramatically decrease the computation time while arriving at the same parameters corresponding to highest performance within the parameter space (assuming no local maxima exist). However, because the parameter space is still user defined, this approach is still limited by the symmetrical objects that the user chooses.

Instead of limiting oneself to the user-chosen, intuitive parameter space, one would rather want to explore the full parameter space in a directed fashion to also allow for unintuitive solutions to the problem. Since 2010, the Vuĉković group at Stanford University showed that their inverse design algorithm was capable of designing unintuitive dielectric structures based only on specified target fields of the light that moves through the structures [19, 26–30]. This method is based on the premise that "any linear optical device can be described by the coupling between sets of input and output modes" [31]. The performance of the structure is defined as the conversion efficiency between input and output modes (Figure 3.1), specifying the input mode as the incoming light and the output mode as the desired outcoming light. Representing the input modes $i = 1...M$ at frequencies ω_i by their current density distributions $\boldsymbol{J_i}$, we find the electric fields $\boldsymbol{E_i}$ generated by these input modes by satisfying Maxwell's equations in the frequency domain,

$$(\nabla \times \mu_0^{-1} \nabla \times - \omega_i^2 \epsilon) \boldsymbol{E_i} = - i \omega_i \boldsymbol{J_i}, \tag{3.1}$$

with ϵ the electric permittivity and μ_0 the magnetic permeability of free space. Then we can specify N_i output modes for each input mode i, with electric fields $\mathscr{E}_{ij}$ defined over output surfaces S_{ij}, where $j = 1 \dots N_i$. The performance, defined as the conversion efficiency between input and output modes, is then specified by the overlap integrals between the input and output modes [28], being constrained as

$$\alpha_{ij} \leq \left| \iint_{S_{ij}} \mathscr{E}_{ij} \cdot \boldsymbol{E_i} \, dS \right| \leq \beta_{ij}. \tag{3.2}$$

Having specified the input fields and constraints on the output fields, the inverse design problem consists of finding the ϵ and $\boldsymbol{E_i}$ that satisfy equations (3.1) and (3.2). Additionally, ϵ has a continuous constraint in the form of $\epsilon_{min} \leq \epsilon \leq \epsilon_{max}$, after which a discretization step is needed to ensure that the design is manufacturable.

The inverse design problem is iteratively solved using the 'objective first' method [28], which means that the electric fields $\boldsymbol{E_i}$ are constraint to satisfy the objective, eq. (3.2), while eq. (3.1) is allowed to be violated. Subsequently, the residual of Maxwell's equations is minimized using the 'Alternating Directions Method of Multipliers' (ADMM) optimization algorithm. Solving eq. (3.1) in three dimensions for $\boldsymbol{E_i}$ is done using a finite-difference frequency-domain (FDFD) solver in Matlab, while eq. (3.2) can directly be solved for ϵ in two dimensions (planar structure with fixed height). The output of the algorithm is a matrix of ϵ values that defines the structure and a matrix of magnetic field values obtained by the FDFD solver that defines the output field and the final performance.

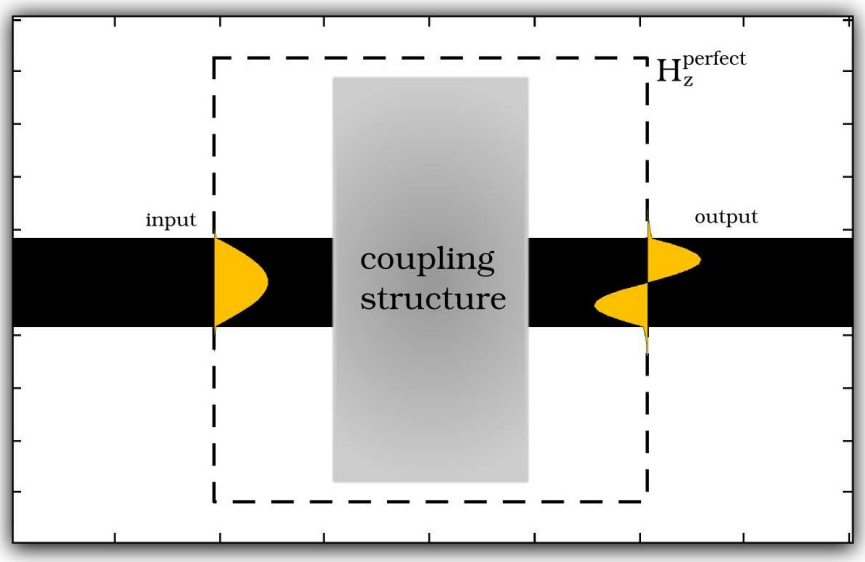

Figure 3.1: *Schematic representation of the definition of input and output fields for the inverse design algorithm. Black rectangles represent the input and output waveguides, with air cladding in white. The structure that is to be optimized is indicated in gray, which is a waveguide coupler in this schematic. Along the dashed line, the fundamental and second-order TE waveguide modes have been specified as the input and output modes (shown in yellow), while the z-component of the target magnetic field ($H_z^{perfect}$) is zero outside the waveguide. (Figure from ref. [27])*

Considering a spectrum-splitting layer that is optically linear, we could envision an inverse designed structure that spectrally splits an incident plane wave or incoming waveguide mode. But before we can work on such a design, we have to understand the behavior of the algorithm as established by the Vuĉković group. A major difference between their work and ours is the operation wavelength: their work is based on integrated photonic devices, which operate in the infrared (1300 - 1550 nm). Therefore, they can work with silicon, which is lossless in this wavelength regime. Recently, they showed that they can inverse design a silicon wavelength demultiplexer, whose objective is to transmit 1300 nm light into output waveguide 1 and 1550 nm light into output waveguide 2, both incoming from the same input waveguide [19]. The simulated and fabricated devices reached the output objective of < 1% transmission into the other output waveguide, but the > 90% transmission objective was not obtained; around 60% of the light was transmitted. Such a performance would be far too low for our purpose of spectrum-splitting the solar spectrum (vertically-stacked tandem solar cells reach external quantum efficiencies of > 90% [7]), which already indicates that we have to change the optimization problem, e.g. by changing the material, the optimization geometry and/or the input source(s).

Employing the inverse design algorithm for the design of a spectrum-splitting layer for the solar spectrum is in principle possible because Maxwell's equations are scale invariant. Scaling down the wavelength would thus imply a smaller structure, which could be constrained to have a minimum feature size to ensure manufacturability. However, silicon is not transparent throughout the visible regime, rendering the use of silicon unfavorable due to high parasitic absorption losses. Instead one could use other high-index materials like SiN_3 or TiO_2 that are transparent to visible light, at the cost of limiting the ϵ to a maximum value of ~4. Before we optimize for a lower maximum ϵ, we will explore the influence of the input parameters of the algorithm for a silicon structure in the following section.

3.2 Inverse design of a silicon waveguide mode converter

In order to understand the behavior of the inverse design algorithm as developed by the Vuĉković group, we chose the waveguide coupling structure problem from Figure 3.1. This problem has been solved in ref. [27], and can thus be easily verified (original Matlab code is available online [32]). The input mode is the fundamental TE waveguide mode and the output mode the second-order TE waveguide mode. Figure 3.2 shows the initial structure (panel a), optimized structure within a box of 40 by 80 pixels (panel b), output magnetic field magnitude (panel c) and amplitude (panel d), obtained after 10.000 iterations. 41.8 grid points correspond to one vacuum wavelength. The conversion efficiency as calculated by the FDFD solver is 99.9%. This value is higher than the 98% reported in ref. [27], because we let the algorithm iterate longer than Lu and Vuĉković . Figure 3.3 shows how the conversion efficiency evolves as a function of iteration, revealing that the conversion efficiency steeply increases. After 100 iterations, the efficiency already exceeds the 90%, whereas after 1000 iterations the efficiency is 99.2%. Although the increase per iteration quickly drops, the conversion efficiency increases with every iteration (except for a small dip around 200 iterations).

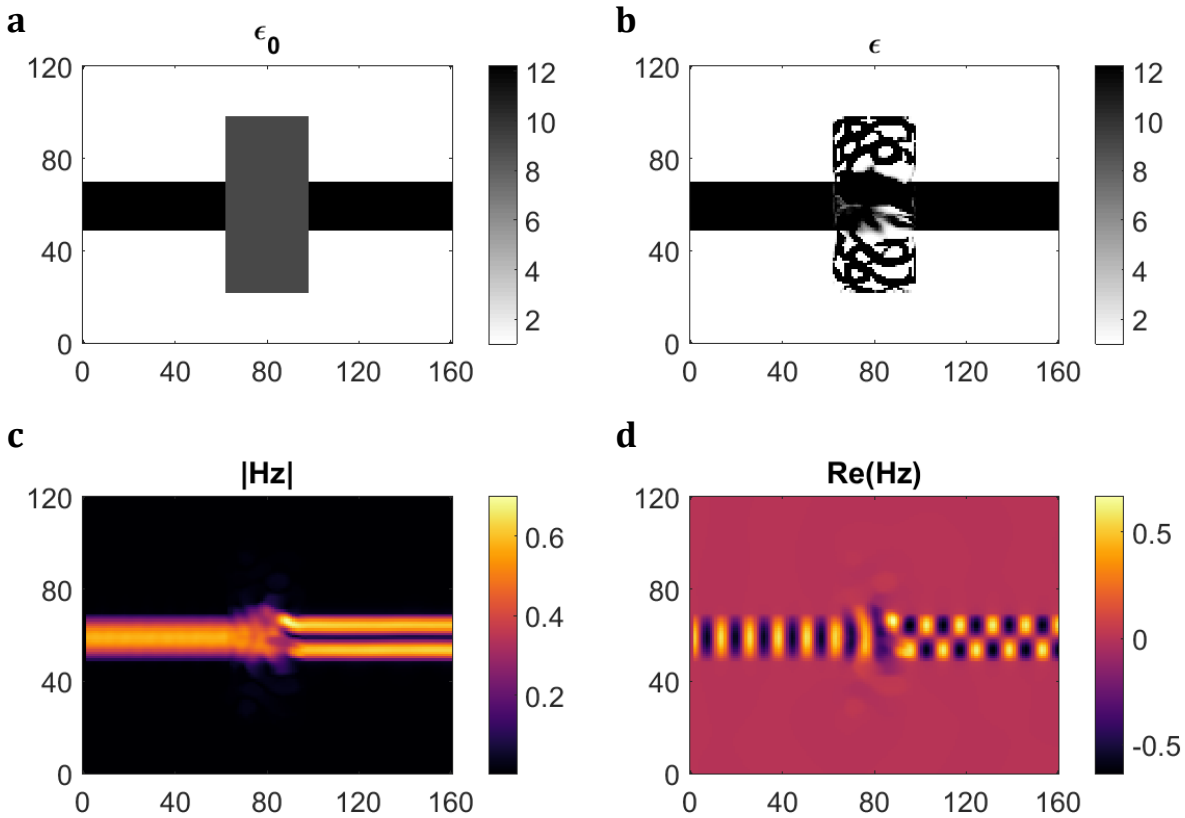

Figure 3.2: *Inverse designed waveguide mode converter. (a) Initial structure, consisting of two silicon waveguides (black, $\epsilon = 12.25$) in air (white, $\epsilon = 1$). A box of 40 by 80 pixels with initial value $\epsilon = 9$ is then optimized using the inverse design algorithm to convert the incoming fundamental TE mode to the second-order TE mode. 41.8 grid points correspond to one vacuum wavelength. (b) Final optimized structure after 10.000 iterations. The structure has continuous varying ϵ values and achieves a calculated conversion efficiency of 99.9%. (c) Calculated magnetic field magnitude using an FDFD solver in Matlab. The conversion from fundamental to second-order TE mode is clearly visible. (d) Calculated magnetic field amplitude, showing a 90° phase shift between the top and bottom parts of the incoming fundamental mode, converting it into a second-order mode.*

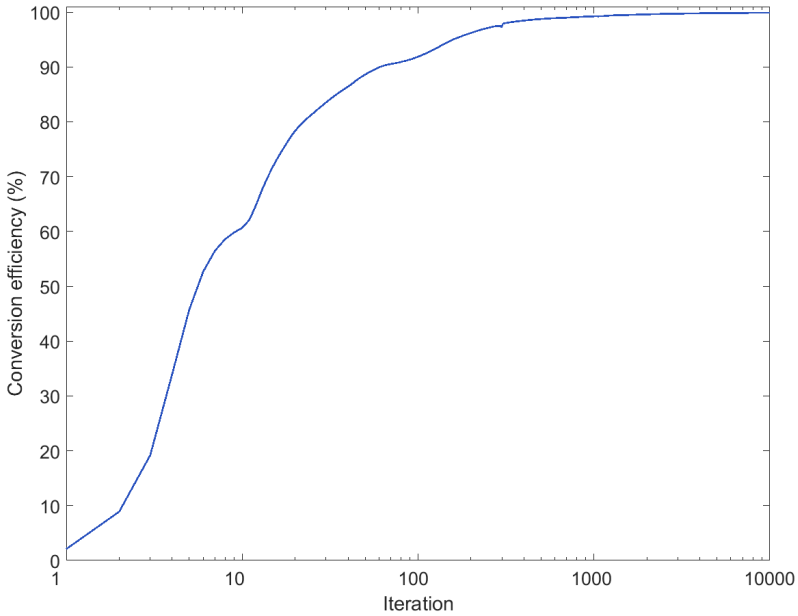

Figure 3.3: *Conversion efficiency as a function of iteration count of the inverse designed waveguide mode converter (see Figure 3.1 for the problem and Figure 3.2 for the final algorithm output after 10.000 iterations). Note that the x-axis has a log scale, which reveals that the conversion efficiency increase per iteration decreases very quickly. Although decreasing, the conversion efficiency increases with every iteration (except for a small dip around 200 iterations), up until 10.000 iterations, where the conversion efficiency increase is roughly a* 10^{-4} *% per iteration.*

The initial value of the electric permittivity in the optimization box is set to 9 (Equation (3.1)), as was used in ref. [27], but this value was arbitrarily chosen, so the effect of this value on the eventual design is discussed in section 3.2.1. Also, because the ϵ values are continuously varying from 1 to 12.25, this design has to be discretized before the performance can be checked by FDTD simulations. The effect of discretization and a subsequent performance check are discussed in section 3.2.2. Because the conversion efficiency is improved very little between 1000 and 10.000 iterations, all consequent results are obtained after 1000 iterations to reduce the computation time.

3.2.1 Initial parameters

One of the input parameters of the inverse design algorithm is initial value of the electric permittivity, ϵ_0, in the optimization box. In their paper, Lu and Vuĉković state that their ϵ_0 values were set to 9, adding: "a somewhat arbitrary guess, other values work as well". Understanding that the ϵ values are modified from their last value to a new value upon each iteration, one might suspect that the initial value would be influencing the optimization at least during the first few iterations. Whether the algorithm always converges to the same result or finds different results for different values of ϵ_0 was not stated in ref. [27] and therefore investigated in this work. Again, the problem of Figure 3.1 was chosen, passing 12 different ϵ_0 values to the algorithm while keeping the other parameters the same. Figure 3.4 shows the final structures after 1000 iterations for ϵ_0 ranging from 1 to 12, and a graph of the conversion efficiency of these structures as a function of their ϵ_0. Comparing the optimized structures, we can see roughly three different types of structures: for ϵ_0 values of 1-4, there is air between the two waveguides, which is surrounded by rings of silicon. ϵ_0 values of 5-7 show some silicon between the waveguides and even more rings of silicon surrounding it. Finally, ϵ_0 values of 8-12 result in a solid connection between the waveguides, surrounded by silicon rings. The performance of the first group is lower than that of the second group, whose performance is consistently above 95%, with maximum performance at 99.7% for $\epsilon_0 = 5$. The third group shows high

performance for ϵ_0 values of 8-10 but less performance for 11 and 12, which differ mainly in the top part of the structure. Another observation that can be made is that most parts of all structures have actually obtained binary values corresponding to minimal and maximal ϵ. Especially the structures of ϵ_0 values 1, 2 and 12 show very little gray areas, while also having significantly lower conversion efficiencies than the others.

Having proven that the initial value of the electric permittivity indeed influences the optimization, we can consider a value in between the extrema of ϵ a good choice to obtain a high-performance structure. The choice of $\epsilon = 9$ made by Lu and Vuĉković is thus good, and indeed other values work as well, although not all values do.

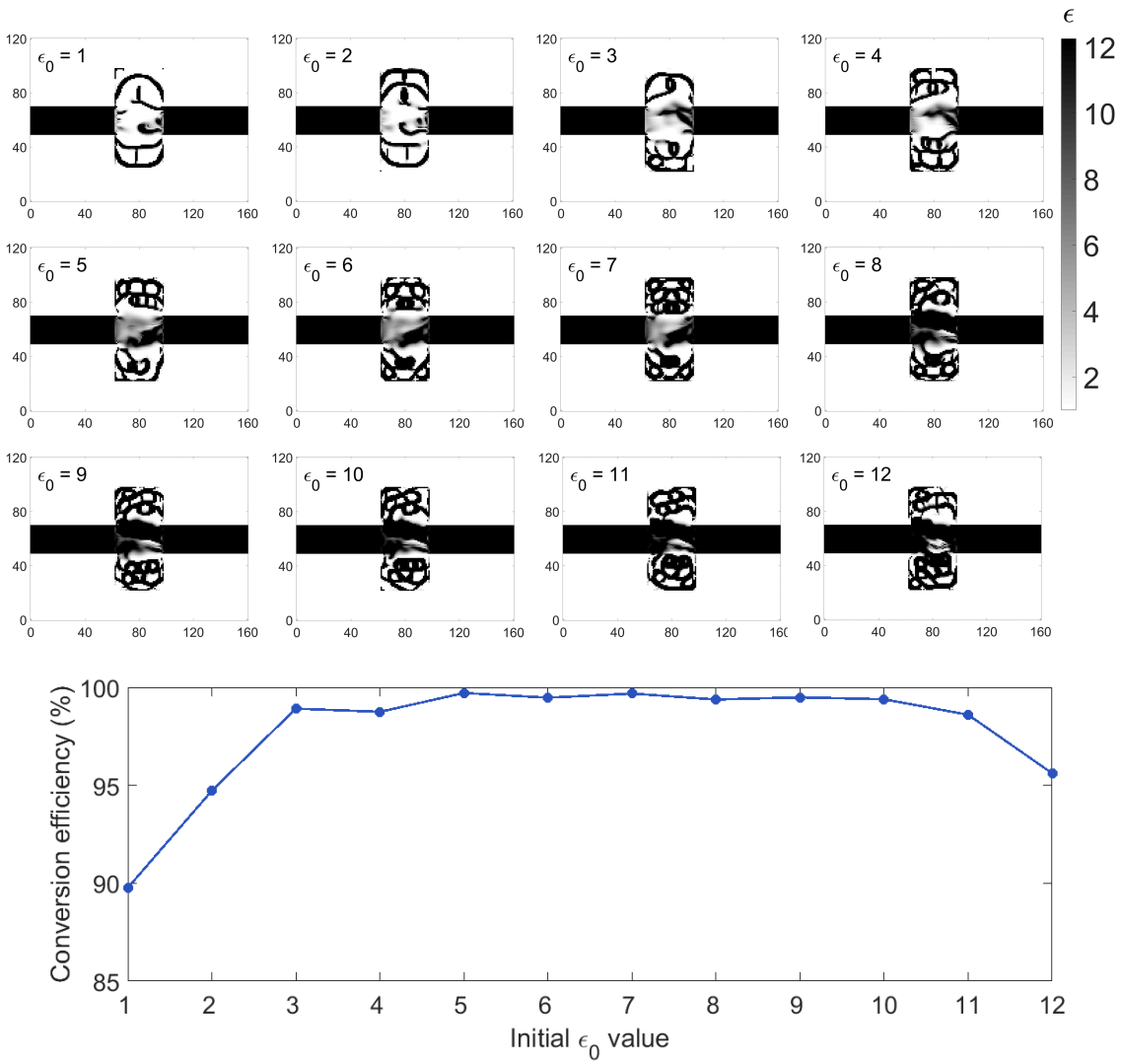

Figure 3.4: *Top: inverse designed waveguide mode converter structures for different initial values of the electric permittivity (ϵ_0) while keeping all other parameters equal to those used in Figure 3.2, after 1000 iterations. Three types of structures can be distinguished based on the filling of the area between the waveguides: little silicon filling (ϵ_0 values 1-4), nearly half silicon filling (5-7), and solid silicon connection (8-12). Bottom: conversion efficiency of the structures shown above as a function of their ϵ_0. Based on their performance, we can distinguish between high-performance structures (3-11) and lower performance (1,2,12). The structures with low performance are also the structures that are most binary in their design, showing little (gray) areas that have ϵ values in between the minimum and maximum.*

3.2.2 Discretization

Although high conversion efficiencies are obtained for the optimized structures, they cannot be fabricated because their ϵ values range between those of air and silicon. Therefore, in order to design a silicon waveguide mode converter, we should discretize the structure its ϵ values to binary values of 1 or 12.25 (corresponding to a refractive index of 3.5). The simplest way of discretizing a grid of values to the boundary values is by imposing a discretization criterion

$$\begin{aligned} &if \qquad \epsilon_i > T \times \epsilon_{max} \qquad \epsilon_i = \epsilon_{max}, \\ &else \qquad\qquad\qquad\qquad \epsilon_i = \epsilon_{min}, \end{aligned} \tag{3.3}$$

with T a discretization parameter having values [0-1], which is user-chosen. Sweeping through all values of T, one can search for the best discretization of the optimized continuous structure. Figure 3.5a shows the conversion efficiency of the waveguide mode converter as a function of discretization parameter T, for the case of $\epsilon_0 = 9$. For $T = 0.36$, the conversion efficiency reaches 92.2%, down from 99.2%. For comparison, Figure 3.5b shows the conversion efficiency as a function of T for $\epsilon_0 = 5$. Similar to the previous case, it peaks at $T = 0.33$, but it reaches only a maximum efficiency of 61.6%, compared to 99.7% for the continuous case. Interestingly, although the two structures perform similarly in the continuous case, they are not at all equally robust against discretization. This shows that the best choice of ϵ_0 is not necessarily the best choice when a binary design is desired. Instead, for each ϵ_0 value, the discretization should be evaluated to find the best combination.

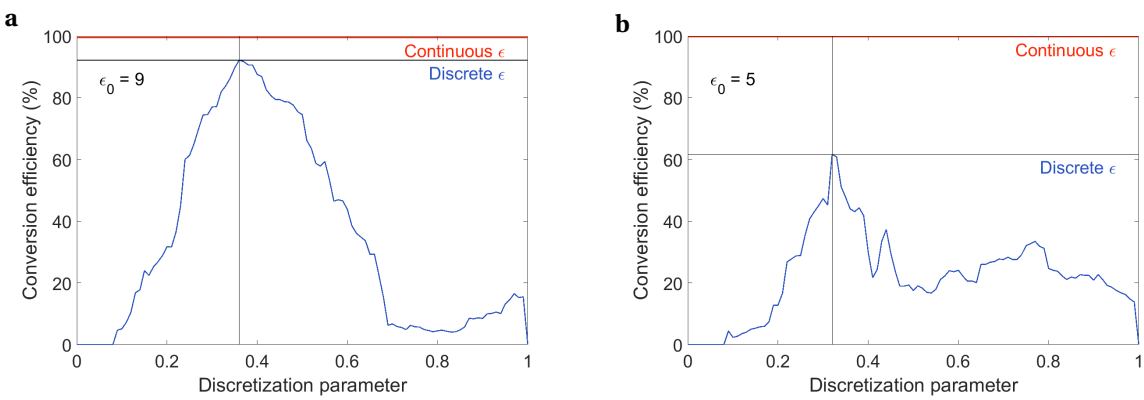

Figure 3.5: *Conversion efficiency of the waveguide mode converter as a function of discretization parameter T after 1000 iterations ($\Delta T = 0.01$). (a) For $\epsilon_0 = 9$, the conversion efficiency drops from 99.2% to 92.2% at $T = 0.36$. (b) For $\epsilon_0 = 5$, the conversion efficiency drops from 99.7% to 61.6% at $T = 0.33$. The difference compared to panel (a) is striking, implicating that a continuous design with a high conversion efficiency is not necessarily a good candidate for a discretized design.*

For the best combination of $\epsilon_0 = 9$ and $T = 0.36$, Figure 3.6 shows the initial structure (panel a), discretized, optimized structure (panel b), output magnetic field magnitude (panel c) and amplitude (panel d), obtained after 1000 iterations. The conversion efficiency as calculated by the FDFD solver is 92.2%, 7% lower than the continuous version shown in Figure 3.2. We checked the performance as calculated by the FDFD solver with an FDTD performance simulation using Lumerical FDTD Solutions, which is widely used in our group (see section 2.3). The optimized and discretized structure shown in Figure 3.6b, was imported into Lumerical (Figure 3.7a shows a top view of the FDTD simulation). The structure was given the appropriate dimensions (5920×4440 nm^2 simulation box, corresponding to 160×120 pixels at 41.8 pixels per 1550 nm vacuum wavelength) and material properties ($n = 3.5$, as a model for silicon, which is lossless at 1550 nm wavelength). A ModeSource was used to excite the fundamental TE waveguide mode in the in-coupling waveguide. Subsequently, the appropriate ModeExpansion and field monitors were used to calculate the magnetic field amplitude and distinguish between different waveguide modes in the out-coupling waveguide for the

conversion efficiency calculation. In Figure 3.7b, the magnetic field amplitude calculated by FDTD is plotted for comparison with Figure 3.6d, which shows very good agreement. The corresponding conversion efficiency into the second-order TE waveguide mode calculated with FDTD is 92.13%, showing excellent agreement between the FDFD and FDTD calculations. Performances calculated with the FDFD solver, which is part of the inverse design algorithm, are thus valid.

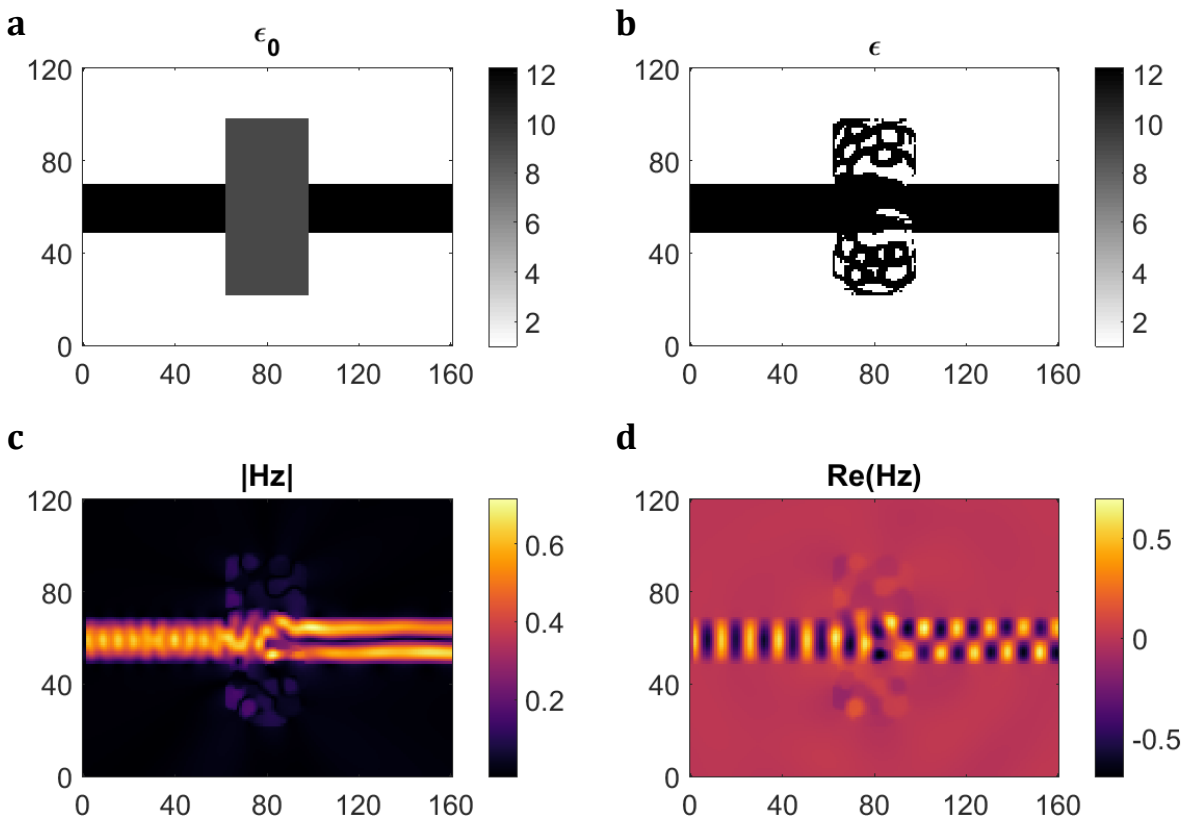

Figure 3.6: *Inverse designed, discretized waveguide mode converter. (a) Initial structure, consisting of two silicon waveguides (black, ϵ = 12.25) in air (white, ϵ = 1). A box of 40 by 80 pixels with initial value ϵ = 9 is then optimized using the inverse design algorithm to convert the incoming fundamental TE mode to the second-order TE mode. 41.8 grid points correspond to one vacuum wavelength. (b) Final optimized structure after 1000 iterations and a discretization step according to eq.* (3.3)*. The structure has binary ϵ values corresponding to silicon and air, and achieves a calculated conversion efficiency of 92.2%. (c) Calculated magnetic field magnitude using an FDFD solver in Matlab. The conversion from fundamental to second-order TE mode is clearly visible. (d) Calculated magnetic field amplitude, showing a 90° phase shift between the top and bottom parts of the incoming fundamental mode, converting it into a second-order mode.*

Because 41.8 pixels correspond to one vacuum wavelength, the pixel size is ~37 nm, rendering the structure manufacturable with current e-beam lithography systems. Because experimental proof of the performance of similar inverse designed structures has already been published [19, 29, 30], we decided not to fabricate the design. Now that we understand and are able to employ the inverse design algorithm, we would want to use it to design a structure that will spectrally split the visible spectrum. In order to do this, we will first have to test the behavior of the algorithm at lower ϵ values (ϵ = ~4), corresponding to materials that are lossless in the visible spectrum such as titanium oxide (TiO_2) or silicon nitride (SiN_3). The next section describes the behavior of the algorithm when ϵ = 4 is used. However, within this project, we have not expanded the algorithm to optimize for multiple wavelengths at ϵ = 4.

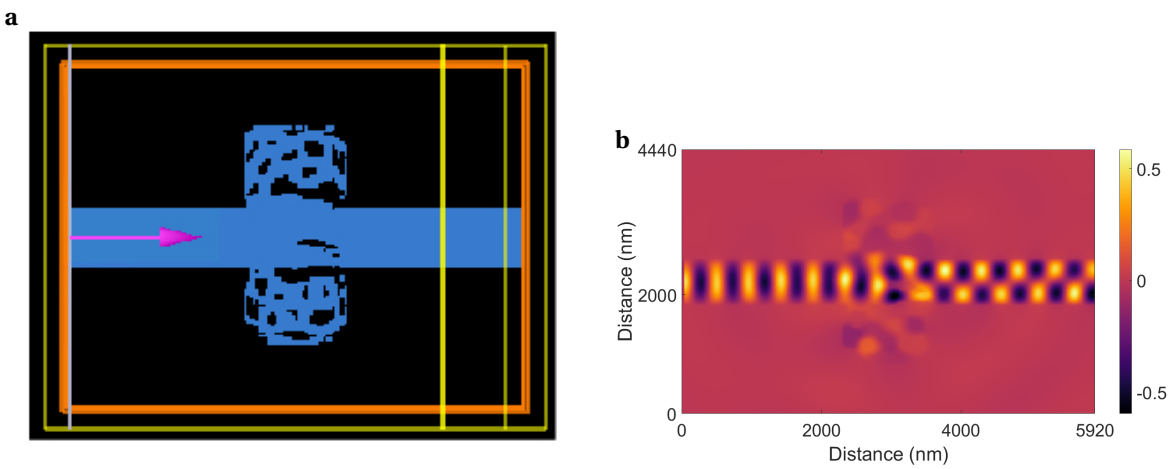

Figure 3.7: *FDTD simulation of the conversion efficiency of the inverse designed waveguide mode converter shown in Figure 3.6b. (a) Top view of the 2D FDTD simulation in Lumerical. The imported inverse designed structure (blue) is surrounded by vacuum (black) and confined by the perfectly matched layers (orange box). A ModeSource source (white vertical line) injects a fundamental TE waveguide mode into the incoupling waveguide (purple arrow). A monitor calculates the total transmission into the outcoupling waveguide (rightmost yellow vertical line), which is decomposed in the different modes present in the waveguide by a ModeExpansion monitor (leftmost yellow vertical line). Finally, a field monitor is placed over the complete simulation area to calculate the magnetic field magnitude of the light as it travels through the structure. The simulation has been checked on convergence as a function of the mesh size, converging at 5 nm meshing. (b) FDTD simulation of the magnetic field amplitude, visually showing the same result as in Figure 3.6d. This simulation was performed by importing the final structure into Lumerical FDTD Solutions. The injected fundamental TE mode was excited at a single wavelength of 1550 nm. The structure was imported accordingly, resulting in a simulation area of 5920 × 4440 nm^2 (160 × 120 pixels). By tracking the transmission of the different modes in the output waveguide, we obtain a transmission of 92.13% for the second-order mode, confirming the conversion efficiency calculation by the FDFD solver.*

3.3 Inverse design of a SiN_3 waveguide mode converter

Because the behavior of the inverse design algorithm has never been investigated at ϵ values other than that of lossless silicon in air (ϵ = [1-12.25]), we decided to take an understood problem and convert from silicon to SiN_3 (modeling it as $\epsilon = 4$). This implicates that the waveguide modes have a longer effective wavelength as compared to the silicon case because the wavelength in a medium is related to the vacuum wavelength as $\lambda = \lambda_0/\sqrt{\epsilon}$. Again we solve the waveguide mode converter problem, keeping all other parameters the same. Because of the previously found importance of ϵ_0, we solve the problem for 7 different ϵ_0 values. Figure 3.8 shows the final optimized structures for these 7 cases (top), as well as the conversion efficiency for each case (bottom). Note that the structures look very binary in their design, but actually still contain some continuously varying ϵ areas. The structures designed with low ϵ_0 values (1-2.5) contain less material than those designed with high ϵ_0 (3-4). The two regimes can also be distinguished regarding the conversion efficiency; lower ϵ_0 values correspond to significantly higher conversion efficiencies. However, the conversion efficiency is far lower than that of its silicon counterpart, reaching a maximum of 73.1% at $\epsilon_0 = 1.5$.

Because we obtain lower conversion efficiencies for the SiN_3 waveguide converter compared to the silicon version, we cannot straightforwardly use the inverse design algorithm to optimize for structures at these ϵ values. Instead, we should alter the optimization problem, for instance by changing size of the optimization box or by changing from a waveguide mode source to a plane wave source. Because of the investigative nature of this project, we have not worked on such a major modification

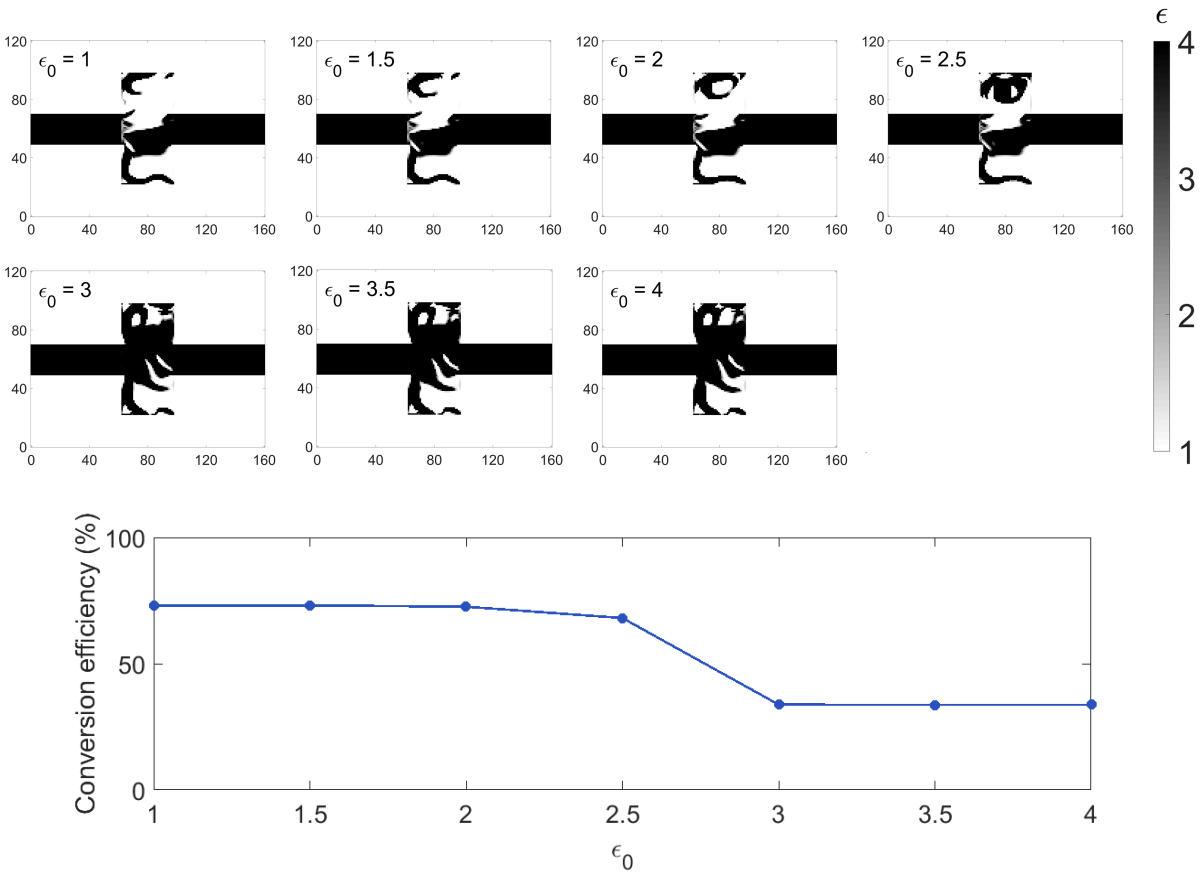

Figure 3.8: *Top: inverse designed waveguide SiN_3 mode converter structures for different initial values of the electric permittivity (ϵ_0), after 1000 iterations. Two types of structures can be distinguished: partly SiN_3 connection (ϵ_0 values 1-2.5), and solid SiN_3 connection (3-4). All structures have a solid 'tail' in the bottom part of the optimization box. Bottom: conversion efficiency of the structures shown above as a function of their ϵ_0. Based on their performance, we can also distinguish the two types of structures: high-performance corresponding with partly filled structures (1-2.5) and lower performance for solidly filled structures (3-4). Maximum performance of 73.1% is obtained for $\epsilon_0 = 1.5$, which is significantly lower than the 99.2% that is reached by the silicon version after 1000 iterations.*

of the algorithm, but instead put effort into a third project, as discussed in Chapter 4. However, we did check the robustness of the SiN_3 waveguide mode converter to a discretization step for either of the two regimes found in Figure 3.8. Figure 3.9 shows the conversion efficiency as a function of the discretization parameter T, defined in eq. (3.3), for the cases of $\epsilon_0 = 1.5$ (panel a) and $\epsilon_0 = 3.5$ (panel b). In contrast to the silicon waveguide mode converter, the SiN_3 design reaches a maximum conversion efficiency that is (slightly) higher than the continuous version. For $\epsilon_0 = 1.5$, the conversion increases marginally by 0.3% to 71.4% at $T = 0.32$, while for $\epsilon_0 = 3.5$ the increase is significant: from 33.7% to 39.4%. This proves that the SiN_3 structure is actually much more robust to discretization than the silicon version, which can be a useful property if a change in the optimization problem could lift the conversion efficiency to near unity. Figure 3.10 shows the output for the highest conversion efficiency obtained for the SiN_3 waveguide mode converter. Compared with the silicon waveguide converter, it can be seen that more light leaks away towards the top and bottom. Note that less optical cycles of the waveguide modes fit in the structure compared with the silicon waveguide mode converter, because the electric permittivity is significantly lower.

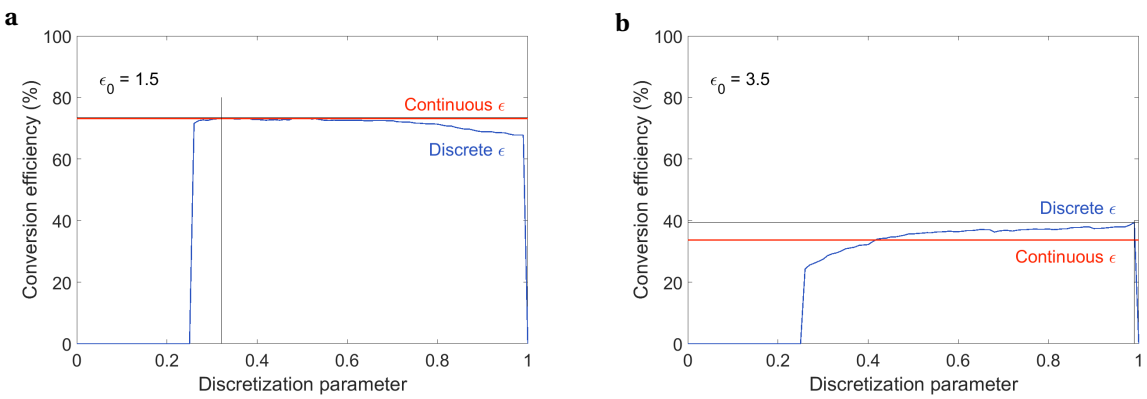

Figure 3.9: *Conversion efficiency of the SiN_3 waveguide mode converter as a function of discretization parameter T after 1000 iterations. (a) For $\epsilon_0 = 1.5$, the conversion efficiency increases from 73.1% to 73.4% at $T = 0.32$. (b) For $\epsilon_0 = 3.5$, the conversion efficiency increases significantly from 33.7% to 39.4% at $T = 0.99$. In contrast to the silicon waveguide mode converter, the SiN_3 version is very robust to discretization.*

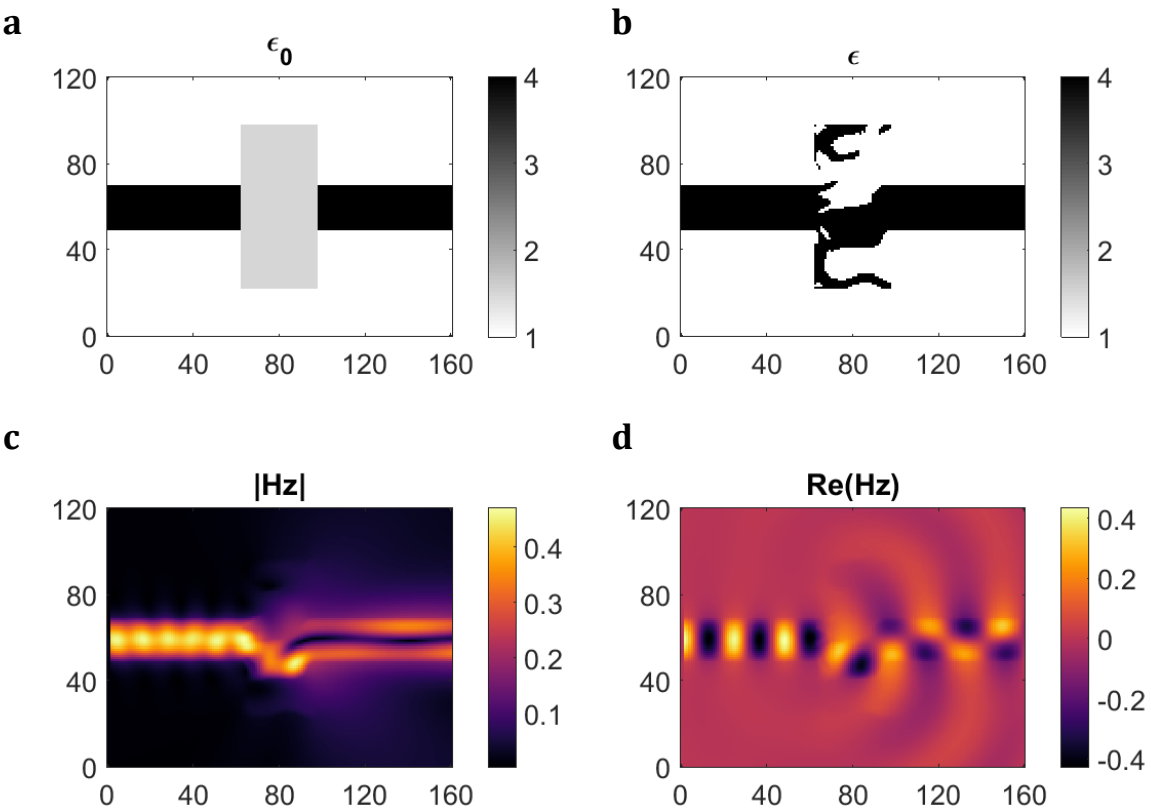

Figure 3.10: *Inverse designed, discretized SiN_3 waveguide mode converter. (a) Initial structure, consisting of two SiN_3 waveguides (black, $\epsilon = 4$) in air (white, $\epsilon = 1$). A box of 40 by 80 pixels with initial value $\epsilon = 1.5$ is then optimized using the inverse design algorithm to convert the incoming fundamental TE mode to the second-order TE mode. 41.8 grid points correspond to one vacuum wavelength. (b) Final optimized structure after 1000 iterations. The structure has been discretized at $T = 0.32$ (see Figure 3.8), and achieves a calculated conversion efficiency of 73.4%. (c) Calculated magnetic field magnitude using an FDFD solver in Matlab. The conversion from fundamental to second-order TE mode is clearly visible. (d) Calculated magnetic field amplitude, showing a 90° phase shift between the top and bottom parts of the incoming fundamental mode, converting it into a second-order mode.*

3.4 Conclusion and outlook

In this work, we have shown that the performance of an inverse designed waveguide mode converter decreases when the structure with continuous varying ϵ values is converted to discrete, binary epsilon values. This conversion is needed if a structure is to be manufactured by two materials, but this necessity results in a decrease from 99.2% to 92.2% conversion efficiency. Consequently, we have changed the material considered in the algorithm from silicon (the sole material considered in previous works) to (SiN_3), by limiting the ϵ range to [1-4]. This change in material results in a decrease in the performance, from 99.2% to 73.1% after 1000 iterations. However, the optimized SiN_3 waveguide mode converter is much more robust to discretization, showing a slightly enhanced performance of 73.4%.

The aim of this work was to understand the inverse design algorithm and characterize the performance of the algorithm when SiN_3 is used instead of silicon. This is of importance before a modification of the algorithm is developed that optimizes a spectrum splitting structure made of SiN_3 . Starting from the silicon waveguide mode converter as published by Lu et al. [27], we learned that the optimization problem should be altered to find out whether near unity conversion can also be achieved with a SiN_3 waveguide mode converter. This change in the optimization problem should either be a change in the optimization box and/or the inputs/outputs, or a change in the problem itself: changing from a waveguide mode problem to a plane wave problem for example. When an optimization problem can be defined that achieves high efficiency using (SiN_3), we can try to optimize a structure for multiple wavelengths that are directed to different output ports, as has been done using silicon by Piggott et al. [19]. In their work, the conversion efficiency suffers from the multiple wavelength objective. Therefore it is essential that a structure that is optimized for a single wavelength objective achieves high efficiency, before trying a multiple wavelength objective. Next year, our group will start working on such a single wavelength, high-efficiency SiN_3 light manipulating structure, with the ultimate goal of inverse designing an efficient, broadband visible wavelength demultiplexer. Instead of working on this already within this master project, we decided to investigate the third approach to a spectrum-splitting layer for tandem solar cell application, which is described in Chapters 4 and 5.

4

Tapered waveguide spectrum-splitter

In pursuit of a spectrum-splitting layer for parallel-stacked tandem solar cells, this work predicts and simulates the spectrum-splitting capabilities of an asymmetric thin-film waveguide that is tapered down to zero in height. While sustaining waveguide modes in the flat region of the film, the waveguide modes reach cutoff as the height is decreased and radiate out of the waveguide, first into the substrate and later also into the air space. The cutoff thickness depends on the wavelength and on the mode order of the waveguide mode, implicating that the wavelength of the radiation into the substrate decreases as the thickness of the waveguide is tapered down. This renders the tapered waveguide a spectrum-splitter when a single mode order is concerned. This chapter introduces the theoretical framework of light confinement in and radiation out of a waveguide, first from the perspective of ray optics and then from wave theory. From both perspectives, the spectrum-splitting is predicted for a titanium oxide (TiO_2) waveguide on a glass substrate. Finally, spectrum-splitting by the same tapered waveguide is simulated using FDTD simulations, showing that the light is radiated into the substrate only, within a narrow range of angles with respect to the TiO_2-glass interface. This serves as a proof of concept for the use of a tapered waveguide as a spectrum-splitting layer for parallel-stacked tandem solar cells. Chapter 5 covers the fabrication and analysis of our TiO_2 tapered waveguides.

4.1 Introduction

If it were easy to employ a tapered waveguide as the spectrum-splitting layer of a parallel-stacked tandem solar cell, it would look like the schematic in Figure 4.1. This figure illustrates the collection of the solar spectrum, which is channeled into a waveguide and reaches the tapered waveguide end where it gets spectrally split. Along the length of the taper from thick to thin, light radiates into the substrate with low to high energy respectively. Underneath, solar cells are stacked parallel to each other, with bandgaps that match the energy of the light at each spot.

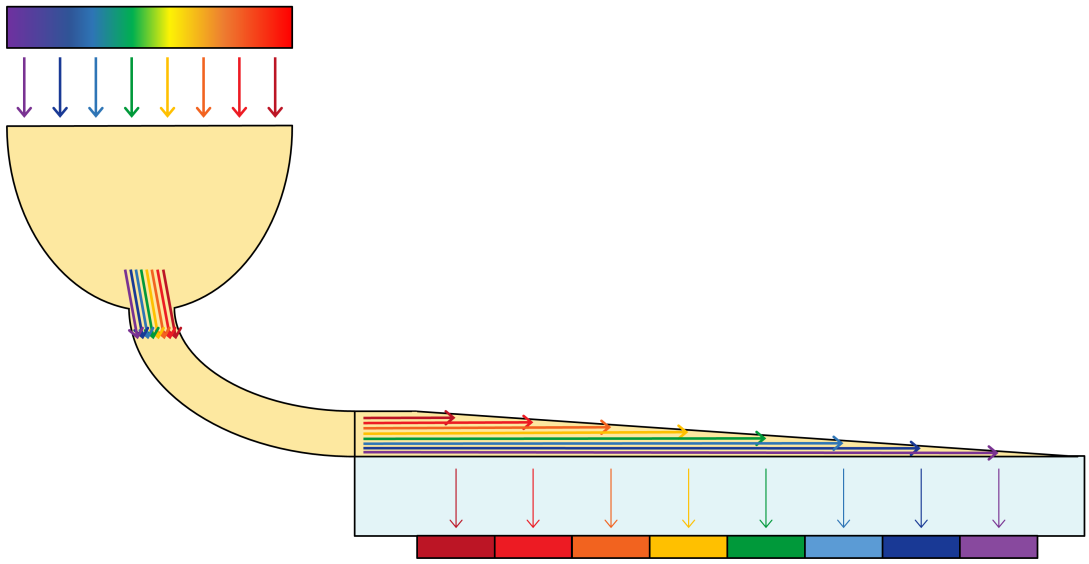

Figure 4.1: *Simplistic schematic representation of a parallel-stacked tandem solar cell that uses a tapered waveguide as its spectrum-splitting layer. Sunlight is collected and channeled into a waveguide. A tapered waveguide spectrally splits it and radiates the light to solar cells underneath it with bandgaps matching the energy of the light. Although an important part of the design is the collection and channeling of sunlight into a wavguide, we will only concern ourselves with the spectrum-splitting capabilities of the tapered waveguide.*

Although a very important part of the design, we will not in this work concern ourselves with the collection of the sunlight, nor how we can efficiently channel it into a waveguide. Instead, we will work out how precisely the tapered waveguide spectrally splits light, first from a ray optics perspective, and later from wave theory. Finally, we will demonstrate spectrum-splitting by a titanium oxide (TiO_2) tapered waveguide using FDTD simulations.

4.2 Waveguide theory

4.2.1 Ray optics description of light propagation in an optical waveguide

The propagation of light waves in planar optical waveguides can be described using a simple ray-optics model. From this perspective, Figure 4.2 depicts the criteria for the guiding of light waves in an asymmetric optical waveguide, consisting of a dielectric film (n_1), on top of a substrate (n_0), with an air cover (n_2) [33]. We define $n_1 > n_0 > n_2$. In the ray optics description, we use Snell's law to relate the angles of the light rays within the three layers with respect to the normal ($\theta_0, \theta_1, \theta_2$),

$$\begin{aligned} n_2 \sin(\theta_2) &= n_1 \sin(\theta_1), \\ n_1 \sin(\theta_1) &= n_0 \sin(\theta_0). \end{aligned} \tag{4.1}$$

Figure 4.2a depicts the *air mode*, corresponding to

$$0 < \theta_1 < \sin^{-1}(n_2/n_1), \tag{4.2}$$

with $\sin^{-1}(n_2/n_1) = \theta_{c_{air}}$ the critical angle for refraction from the film to air. In this case, light originating from the film can refract into both the substrate and air. Increasing θ_1 to a value larger than the critical angle for the air cover,

$$\sin^{-1}(n_2/n_1) < \theta_1 < \sin^{-1}(n_0/n_1), \tag{4.3}$$

with $\sin^{-1}(n_0/n_1) = \theta_{c_{substrate}}$, we reach total reflection at the film-air interface because we reach the impossible condition of $\sin(\theta_2) > 1$. This corresponds to the *substrate mode* shown in 4.2b, where refraction is retained at the film-substrate interface. Increasing θ_1 further to a value larger than $\theta_{c_{substrate}}$,

$$\sin^{-1}(n_0/n_1) < \theta_1 < \pi/2, \tag{4.4}$$

we have total reflection at both interfaces, confining the light ray in the film to a *waveguide mode*, as shown in 4.2c. This confinement implicates that the light effectively only travels in the direction parallel to the film because the upward-traveling and downward-traveling rays have equal but opposite vertical components. This causes a standing wave pattern across the thickness of the film. In addition, the upward-traveling and downward-traveling rays have equal and aligned horizontal components, causing the waveguide mode to move with constant speed in the horizontal direction. Changing the angle of the light rays θ_1, we change the horizontal and vertical components of the rays and thus the speed in the horizontal direction and the standing wave pattern in the vertical direction.

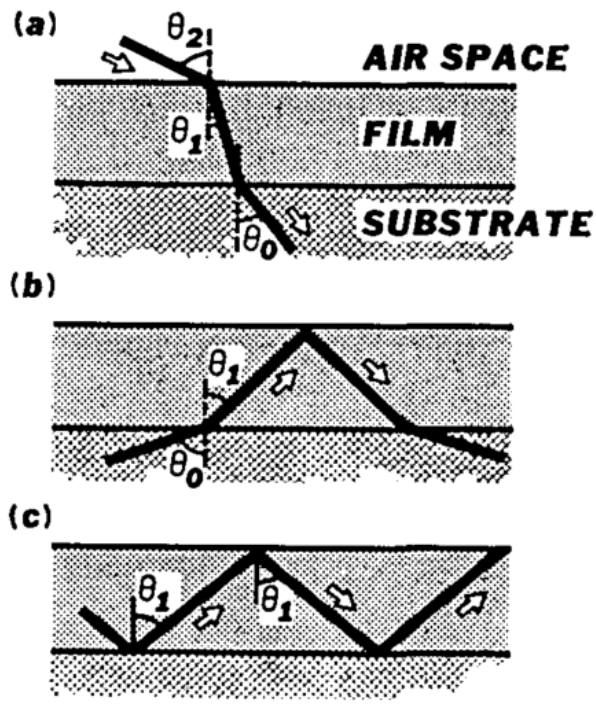

Figure 4.2: *Ray optics description of the confinement of light in an asymmetric optical waveguide. (a) For $\theta_1 < \sin^{-1}(n_2/n_1)$, the light ray can both refract from the film into the substrate and air, which is referred to as the air mode. (b) For $\sin^{-1}(n_2/n_1) < \theta_1 < \sin^{-1}(n_0/n_1)$, we are in the substrate mode regime, where light is totally reflected from the film-air interface, but refracted at the film-substrate interface. (c) For $\sin^{-1}(n_0/n_1) < \theta_1 < \pi/2$, the light is totally reflected from both interfaces, fully confining it to propagation inside the film, which corresponds to a waveguide mode. (Figure from ref. [33])*

Considering multiple reflected light waves inside the waveguide, we find constructive or destructive interference depending on the relative phase difference between any two waves in the vertical direction. Waveguide modes that propagate inside the film must thus fulfill a constructive interference constraint, requiring zero phase difference between the original and reflected waves. For a wave with wave vector k_0, propagating under an angle θ_1 inside the film, the magnitude of the vertical component equals $k_0 n_1 \cos(\theta_1)$. Upon traveling twice (up and down) the thickness of the film, the wave has acquired a phase difference of $2dk_0 n_1 \cos(\theta_1)$, with d the thickness of the film. Incorporating the phase changes acquired upon reflection from the film-air and film-substrate interfaces, Φ_{12} and Φ_{10} respectively [34], we require for constructive interference that

$$2dk_0 n_1 \cos(\theta_1) - \Phi_{12} - \Phi_{10} = 2m\pi, \tag{4.5}$$

where the RHS corresponds to zero phase change upon a double pass through the film, plus m times a full period (2π), and $m = 0, 1, 2, 3, ...$, is the order of the mode. Each waveguide mode that can exist is thus uniquely defined by the thickness d of the waveguide in which it propagates and the wave vector k_0 of the light.

4.2.2 Ray optics description of radiation out of a tapered optical waveguide

Staying in the ray optics description of a waveguide, we can take a look at what happens to the light paths when we change the thickness of the waveguide by tapering it down to 0 over a certain distance (see Figure 4.3). From the previous section, we understood that the thickness d of the waveguide and the propagation angle θ_1 determine whether light with a certain wave vector k_0 is confined within the waveguide. By tapering the waveguide, we decrease d and thereby decrease θ_1 as the waveguide mode propagates through the tapered part of the waveguide. When θ_1 decreases below the critical angle, the light can refract towards the substrate, as shown in Figure 4.3, between points a' and b'. Point C in the figure indicates the thickness for which the guided light moves under the critical angle inside the waveguide, and thus the thickness after which the light will start radiating out of the waveguide into the substrate, which is referred to as the cutoff thickness. The cutoff thickness is calculated by inserting the critical angle $\theta_{c_{substrate}}$ into eq. (4.5):

$$d_{cutoff} = \frac{m\pi}{k_0 n_1 \cos(\theta_{c_{substrate}})}, \tag{4.6}$$

where Φ_{12} and Φ_{10} have decreased to zero at the critical angle [34]. The cutoff thickness thus depends on the mode order m and the wave vector k_0. This dependence gives a tapered waveguide its spectrum-splitting property because light with different wave vectors will couple out of the tapered waveguide at different positions (for equal mode order). In particular, because $k_0 = \frac{2\pi}{\lambda_0}$, the wavelength that starts radiating out will be shorter (blueshifts) as the waveguide thickness decreases.

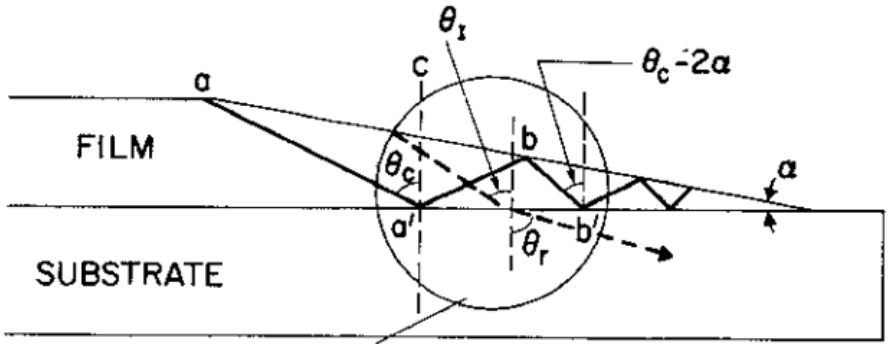

Figure 4.3: *Schematic representation of the light path in a tapered waveguide on a substrate. The film is tapered down to zero, starting at a, under an angle α. At a', the cutoff thickness c is reached, corresponding to the critical angle θ_c for which total reflection occurs at the film-substrate interface. Because of the taper angle α, the angle of incidence changes by -2α when the light ray travels up and down once, as indicated for point b'. At any point to the right of a', the light ray will partially refract into the substrate, as is depicted within the circle by the dashed line: the light ray is incident upon the interface under angle $\theta_I < \theta_c$, and refracts under angle θ_r. (Figure from ref. [35])*

4.2.3 Wave description of light in an optical tapered waveguide

Having described the propagation in and radiation out of a tapered waveguide in a rather intuitive way in the previous sections, we will move to a more mathematically rigorous description by solving Maxwell's equations for an asymmetrical waveguide. Choosing a waveguide film with infinite width in the y-direction, thickness d in the x-direction and propagation in the z-direction, we can solve Maxwell's equations in terms of the electric field in the y-direction, E_y, for TE waveguide modes or the magnetic field in the y-direction, H_y, for TM modes. Choosing the TE modes, we have the wave equation

$$\frac{\partial^2 E_{y,j}(x,z,t)}{\partial x^2} + \frac{\partial^2 E_{y,j}(x,z,t)}{\partial z^2} = -k_0^2 n_j^2 E_{y,j}(x,z,t), \tag{4.7}$$

with $E_{y,j}(x,z,t)$ the electric field in the y-direction and n_j the refractive index, for medium $j = 0,1,2$, corresponding to the substrate, the film, and air, respectively. The solution to the wave equation in the form of

$$E_{y,j}(x,z,t) = e^{-i\omega t}\, e^{ik_{x,j}x}\, e^{\pm ik_{z,j}z} \tag{4.8}$$

can then be substituted into eq. (4.7) to obtain

$$k_{x,j}^2 + k_{z,j}^2 = k_0^2 n_j^2, \tag{4.9}$$

which shows that waves propagating in medium j can be decomposed into a horizontal and a vertical component.

To have a clear differentiation between the propagation direction of the light waves inside the waveguide going up and down, and the effective propagation of the waveguide mode in the z-direction, it is useful to define the latter by the propagation constant β as

$$\beta = k_0 n_1 \sin(\theta_1), \tag{4.10}$$

which is a unique property of each waveguide mode with a certain wave vector. Boundary conditions at the two interfaces require the parallel wave vectors in the different media to be equal, so we can substitute $k_{z,j} = \beta$ into eq. (4.9) to obtain

$$k_{x,j} = (k_0^2 n_j^2 - \beta^2)^{\frac{1}{2}}, \tag{4.11}$$

relating the vertical components of the wave vectors in the three media to the free space wave vector k_0 and the propagation constant of a waveguide mode, substrate mode or air mode. Substituting eq. (4.10) into the conditions for the air mode, substrate mode and waveguide mode given in eqs. (4.2) to (4.4), we can now rewrite those as

$$0 < \beta < k_0 n_2, \tag{4.12}$$

$$k_0 n_2 < \beta < k_0 n_0, \tag{4.13}$$

$$k_0 n_0 < \beta < k_0 n_1. \tag{4.14}$$

Having rewritten our mode conditions in terms of β, we can substitute these into eq. (4.11) to obtain the confinement of the waves in the three mode regimes. For the waveguide mode (Equation (4.14)), $k_{x,1}$ is real while $k_{x,0}$ and $k_{x,2}$ are imaginary. This corresponds to a standing wave in the film, and exponential decaying waves in the substrate and air, as expected. Similarly, for the substrate mode (Equation (4.13)), we find standing waves in the film and substrate, and exponential decay in the air space. Finally, for the air mode (Equation (4.12)), we find standing waves in all three media.

These relations provide a very clear distinction between the three different mode regimes that are present in the asymmetric waveguide system and will enable us to easily distinguish between air, substrate and waveguide modes when we solve eq. (4.8) for a TiO_2 waveguide on a SiO_2 substrate in the next section.

4.3 TiO_2 tapered waveguide on a glass substrate

In the previous section, we have introduced the wave equation (Equation (4.7)), that we can now solve to find the modes of an actual system. We choose a TiO_2 waveguide ($n_{TiO_2} = 2.25$ at $\lambda_0 = 600$ nm) on a glass substrate ($n_{SiO_2} = 1.46$ at $\lambda_0 = 600$ nm) in air. Solving the wave equation in the three materials of this asymmetric slab waveguide, we obtain the dispersion relation for the modes in the system. Figure 4.4 shows the dispersion relation for TiO_2 thicknesses of 130 nm (blue), 175 nm (green) and 255 nm (red). For clarity, only the second-order TE modes are considered. The dispersion relation relates the propagation constant β to the wave vector k_0 for each mode. Having quantified the β values for the air, substrate and waveguide modes in eqs. (4.12) to (4.14), we can distinguish between the different modes in the dispersion relation by plotting the three regimes in the same graph

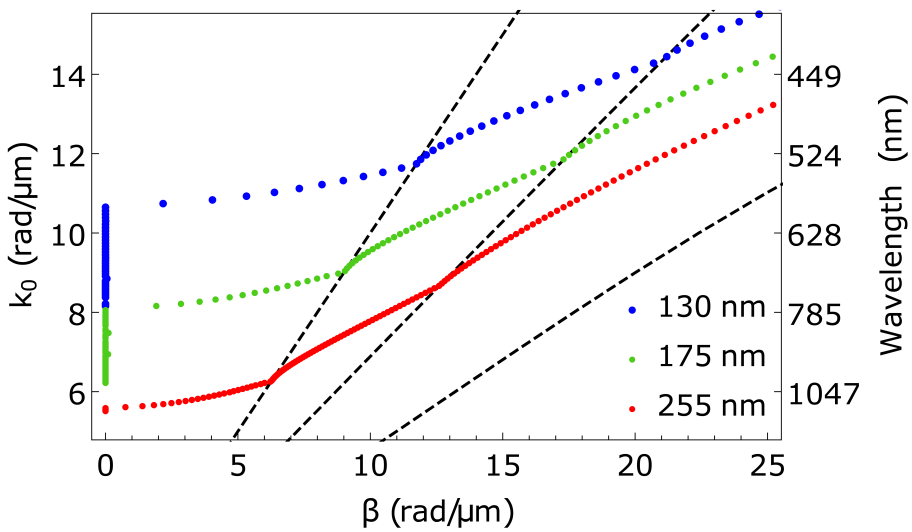

Figure 4.4: *Dispersion relations for a TiO_2 waveguide on a SiO_2 substrate in air, for waveguide thicknesses of 130 nm (blue), 175 nm (green) and 255 nm (red), considering only the second-order TE modes. The dashed lines indicate the regimes of the three different modes that the system sustains, according to eqs.* (4.12) *to* (4.14)*. Waveguide modes are sustained for β values between the two rightmost dashed lines. Substrate modes are present between the two leftmost dashed lines, and air modes are found between the vertical axis and the leftmost dashed line.*

(dashed lines). Waveguide modes are found on the right side, between the two rightmost dashed lines, corresponding to the range of β values in eq. (4.14). Similarly, we find substrate modes between the two leftmost dashed lines and air modes between the vertical axis and the leftmost dashed line.

The dispersion relation for a waveguide of given thickness tells us whether light with a particular wavelength will be confined to the waveguide, can radiate only towards the substrate side, or can radiate towards both the substrate and air sides. Conversely, by computing the dispersion relation for a range of waveguide thicknesses, one can determine for a particular wavelength for which thickness of the waveguide it will be sustaining a waveguide, substrate or air mode. Thus, the confinement of the light is dependent on the waveguide thickness and the wavelength.

As shown in the previous sections, we can convert a waveguide mode to a substrate or air mode by tapering the waveguide. Because of the asymmetry of the waveguide's cladding, the waveguide mode will first become a substrate mode, radiating a part of the energy in the waveguide mode into the substrate each time it hits the film-substrate interface. Because the conversion from a waveguide mode to a substrate mode is dependent on both the thickness of the waveguide and the wavelength, light of different wavelengths will couple out at different thicknesses of the tapered waveguide. From the ray optics perspective, we can directly see from eq. (4.6) that the cutoff thickness d_{cutoff} is inversely proportional to the wave vector k_0, and thus proportional to the wavelength λ_0, for the same mode order m. This causes the tapered waveguide to act as a spectrum splitter when light of different wavelengths in the same mode order is guided into a tapered waveguide. From wave theory, observe the same from the dispersion relation when we consider a single wavelength: decreasing the thickness of the waveguide will convert a waveguide mode to a substrate mode to an air mode (moving horizontally from right to left in the dispersion graph in Figure 4.4).

If we want to use a tapered waveguide as a spectrum splitter for a parallel-stacked tandem solar cell module, it would be most convenient to have only radiation from the tapered waveguide into the substrate, so that we would only have to place solar cells underneath the taper. That would require that all the light has already dissipated from the waveguide into substrate modes before the air modes are opened up. This criterion then limits us to radiation into the substrate under angles that correspond to the substrate mode regime only (Equation (4.3)). Calculating, from the lower bound

for the angle of incidence, the maximum angle of refraction into the substrate, we find $\theta_{0,r} = 43°$ at $\lambda_0 = 600$ nm, with respect to the horizontal.

From the wave theory perspective, we can easily compute the angles of refraction into the substrate from the dispersion relation for each wavelength and waveguide thickness. Figure 4.5 shows these angles of refraction into the substrate with respect to the horizontal (color), as a function of the waveguide thickness and the wavelength. A refraction angle of 0° (blue) corresponds to a waveguide mode, i.e. no radiation into the substrate. From this plot, we see the spectrum-splitting capability of the tapered waveguide, because the radiation into the substrate starts with large wavelengths as we taper the waveguide down from 500 nm to 350 nm. Tapering the waveguide further down, long wavelengths reach their maximum refraction angle slightly above 40°; white color indicates the start of the air modes. As we taper the waveguide down, shorter wavelengths reach their substrate modes and start radiating into the substrate. Note that shorter wavelengths reach their maximum refraction angle quicker as a function of the waveguide thickness, and will thus radiate from a shorter part of the taper when a linearly tapered waveguide is concerned.

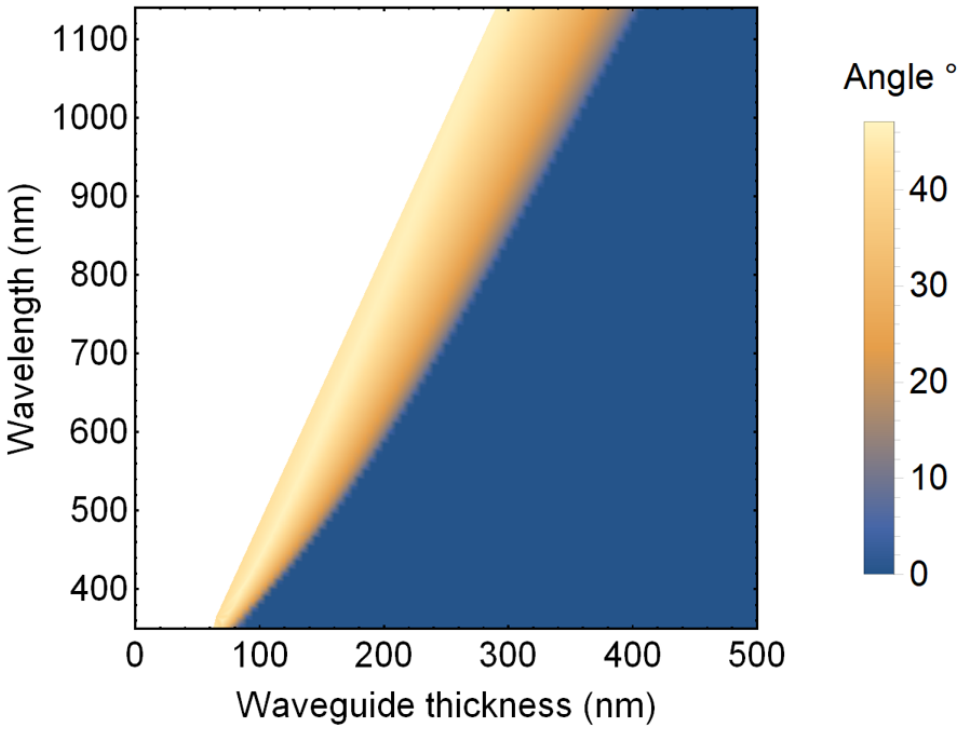

Figure 4.5: *Radiation angles into the substrate with respect to the horizontal (colors), as a function of tapered waveguide thickness and wavelength. 0° (blue) indicates waveguide modes that do not radiate into the substrate. As expected, longer wavelengths start radiating at larger thicknesses; shorter wavelengths at shorter thicknesses. All substrate modes reach their maximum radiation angle slightly above 40°, after which air modes are opened up (white). Note that shorter wavelengths reach their maximum radiation angle quicker as a function of the waveguide thickness.*

Although we have been able to calculate the range of angles under which the taper radiates towards the substrate side, we do not know what the power distribution over the angles will be for a given tapered waveguide. Therefore we will perform FDTD simulations of a tapered waveguide to show that it radiates 100% of the light towards the substrate side, and to determine the power distribution as a function of radiation angle into the substrate.

4.3.1 FDTD simulation of spectrum-splitting by a TiO_2 tapered waveguide

In the previous sections, we have worked out how a tapered waveguide can function as a spectrum-splitter and under what angles the taper can radiate light towards the substrate side if it is constraint from radiating towards the air side. Using FDTD simulations of the TiO_2 waveguide on a glass substrate, as considered in the previous section, we will show that light is only radiated towards the substrate side, enabling us to place solar cells underneath the tapered waveguide.

Figure 4.6 shows a side view of the FDTD simulation area in Lumerical, where the TiO_2 waveguide (red) is placed on a glass substrate (white). A second-order TE mode is injected into the waveguide (purple arrow), and two monitors calculate the power that is radiated towards the substrate (lower yellow horizontal line) and the air side (upper yellow horizontal line). Figure 4.7 shows the calculated power as a function of position along the taper for the top monitor (panel (a)) and the bottom monitor (panel (b)). While panel (b) shows the characteristic spectrum-splitting behavior of the system, measuring shorter wavelengths as the taper gets thinner, panel (a) shows that there is no light radiated towards the air side. Note that panel (b) shows that the confinement of the light in space is higher for shorter wavelengths, as was also observed for the radiation angles towards the substrate side shown in Figure 4.5.

Figure 4.6: *Side view of the 2D FDTD simulation in Lumerical, simulating the spectrum-splitting of a tapered waveguide. The TiO_2 waveguide with a tapered end (red) is placed on top of a glass substrate (white), which both extend through the perfectly matched layers (orange box). A ModeSource source (gray vertical line) injects a second-order TE waveguide mode into the waveguide (purple arrow). Two monitors calculate the power transmitted above and below the tapered waveguide (yellow horizontal lines). The simulation extends further towards the right (the end of the simulation area is not shown), in order to also monitor the light that radiates nearly parallel to the horizontal axis.*

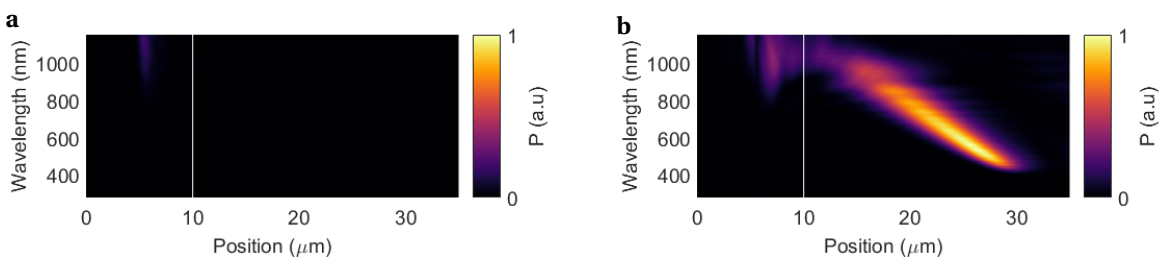

Figure 4.7: *Simulated power (color) as a function of position along the tapered waveguide (horizontal axis) and wavelength (vertical axis). The simulation has been performed as shown in Figure 4.6. The tapered waveguide is 25 µm long and tapered down from 500 nm to 0 nm. The power monitors are placed 200 nm below and above the tapered waveguide. (a) Simulated power above the tapered waveguide, showing that no light is radiated towards the air side. (b) Simulated power below the tapered waveguide, showing the characteristic spectrum splitting behavior for light radiated into the substrate. No signal is observed below 450 nm because TiO_2 is absorbing significantly below this wavelength.*

Now that we simulated the spectrum-splitting behavior of the tapered waveguide using FDTD, we have a proof of principle for the use of a tapered waveguide as the spectrum-splitting layer for a parallel-stacked tandem solar cell. The simplest version of such a tandem is composed of two individual solar cells, a high bandgap and a low bandgap solar cell. Taking several cross-cuts of the power spectrum in Figure 4.7b, we plot the power for several wavelengths as a function of position underneath the taper in Figure 4.8. By drawing a black vertical line roughly halfway along the taper length, we separate the spectrum into two spectral bands. In this fashion, we can place a solar cell on either side of the black line, for instance, a Si solar cell (bandgap at 1107 nm) on the left and a gallium-arsenide (GaAs) solar cell (bandgap at 875 nm) on the right.

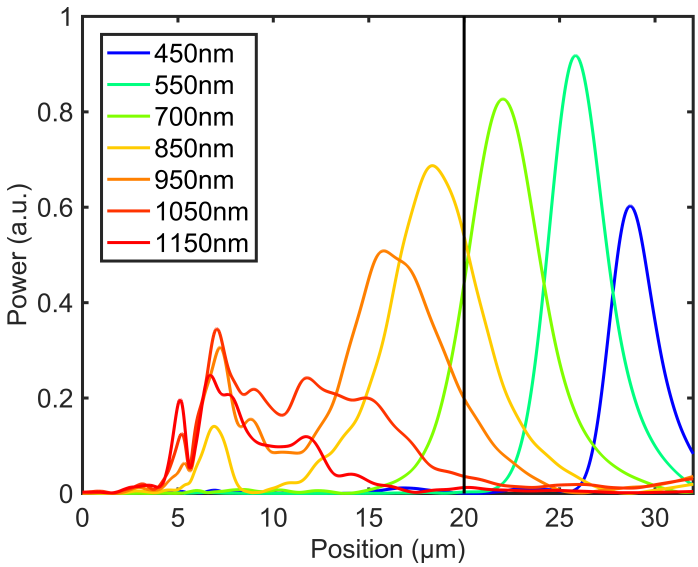

Figure 4.8: *Simulated power radiated into the substrate, as a function of position along the tapered waveguide (horizontal axis) for different wavelengths. The data corresponds to cross-cuts of the color plot shown in Figure 4.7b. The vertical black line is arbitrarily chosen to separate the spectrum into two spectral bands: 450-850 nm to the right and 850-1150 nm to the left. This indicates that the spectrum is already split enough 200 nm below the taper-substrate interface to place to individual solar cells there, for instance, a silicon solar cell (bandgap at 1107 nm) to the left of the black vertical line and a gallium-arsenide solar cell (bandgap at 875 nm) to the right.*

Although we find spectrum-splitting behavior in FDTD simulations right below the waveguide-substrate interface, we do not know what the power distribution is over de radiation angles. Therefore we used the near to far field projection that is available in Lumerical to calculate the far field radiation pattern for each wavelength. Figure 4.9 shows the far field radiation patterns for three wavelengths, 450, 700 and 950 nm, which look very much alike and are representative of all radiation patterns corresponding to wavelengths between 450-1150 nm. From this graph, we learn that nearly no light is radiated into the substrate under angles of 0-10°. Then all of the light is radiated between 10-20°, with a peak around 15°. This means that the power spectrum we obtained in Figure 4.7 will keep its shape as we move further down below the tapered waveguide, only shifting to the right under an angle of about 15°.

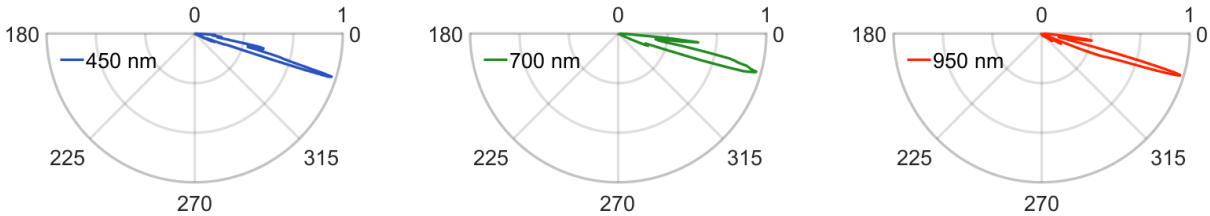

Figure 4.9: *Farfield radiation patterns of light radiated from the simulated tapered waveguide shown in Figure 4.6, for wavelengths of 450, 700 and 950 nm. Using the near to far field projection available in Lumerical, we calculated the far field radiation from the near field power that was calculated as described for Figure 4.7. The power distribution over the radiation angles is very inhomogeneous: until about 10° little light is radiated into the substrate. Then the radiation peaks at 15°, and after 20° nearly no light is radiated anymore. The spectra showed here look a like, and are representative for all angles between 450-1150 nm (below 450 nm TiO_2 is absorbing).*

4.4 Conclusion

In this work, we have theoretically derived the spectrum-splitting properties of a tapered waveguide using ray optics and wave theory for an asymmetric waveguide. Using ray optics, we explained intuitively that light inside a waveguide will first radiate towards the substrate side before it can radiate towards the air side. Subsequently, using wave theory, we calculated the dispersion curves for each thickness of a TiO_2 tapered waveguide on a glass substrate to find the wavelengths of the waveguide, substrate and air modes for each thickness. From these dispersion curves, we computed the radiation angles under which the light can radiate into the substrate once it surpasses its cutoff thickness. Finally, we verified the expected spectrum-splitting by simulating the TiO_2 tapered waveguide using FDTD simulations. We found that no light was radiated towards the air side for a short taper of 25 μm long and 500 nm thick. In contrast, with decreasing thickness of the waveguide, shorter wavelengths were radiated towards the substrate side, as expected. In addition, using the near to far field projection of Lumerical, we found that nearly all light was radiated towards the substrate side under angles of 10-20° with respect to the horizontal. This means that the light keeps its spectrum-split shape as it moves down.

The calculations and simulations that are described in this chapter were carried out to determine the spectrum-splitting capabilities of a TiO_2 tapered waveguide. After a proof of concept was obtained by means of FDTD simulations, we started fabrication of a TiO_2 tapered waveguide on a glass substrate to experimentally verify the spectrum-splitting behavior. The fabrication process and experimental setup are described in chapter 5.

5

Tapered waveguide fabrication and measurements

Based on the theoretical understanding and simulations of the tapered waveguide, as described in chapter 4, we fabricated two TiO_x tapered waveguides on a glass substrate. This chapter first describes the e-beam physical vapor deposition method used for the fabrication. Then the analysis methods used to characterize the taper geometries are described. We show that the taper has a linear slope and that we can determine the final TiO_x thin film thickness from reflection measurements because of the exhibited Fabry-Pérot resonances. Finally, we describe the scanning near-field optical microscopy (SNOM) setup we employed to experimentally probe the spectrum-splitting behavior of the tapered waveguide inside the glass substrate. However, due to incorrect extrapolation of the results from FDTD simulations, this setup was not able to measure the effect. Therefore, two alternative experimental setups are described, based on the insights gained from the SNOM setup, that we will build in future work to demonstrate the spectrum-splitting behavior of the tapered waveguide.

5.1 Fabrication of a TiO_2 tapered waveguide

Based on the theory and simulations described in chapter 4, we fabricated two TiO_2 tapered waveguides on a glass substrate using e-beam physical vapor deposition (EB-PVD). Figure 5.1 shows a schematic of the EB-PVD thin film growth technique, which takes place in a vacuum chamber (base pressure: 1.6×10^{-6} mbar). Inside the crucible holder, a crucible is placed that contains the precursor material. In our case, we want to grow a TiO_2 film, for which we use Ti_3O_5 as precursor. In vacuum, the precursor is heated by means of an electron beam, to create precursor vapor in the vacuum chamber. The vapor spreads through the chamber and precipitates onto the substrate that is positioned above the crucible. By controlling the electron beam current and measuring the deposition of material as a function of time on a piezoelectric actuator next to the glass substrate, we adjust the electron beam to keep the deposition rate constant. The exact deposition rate is not known, but based on deposition rate calibrations of previous TiO_x depositions, the deposition rate is expected to be around 1 Å/s. To create a homogeneous and near stoichiometric TiO_2 thin film, we flow extra O_2 gas into the vacuum chamber (base pressure: 1.6×10^{-5} mbar). To create a tapered waveguide on one side of the film, we place a slow shutter in front of the substrate. By moving the slow shutter during deposition parallel to the substrate away from it, we create a time varying 'shadow', effectively decreasing the thickness of the deposited film towards the edge of the substrate.

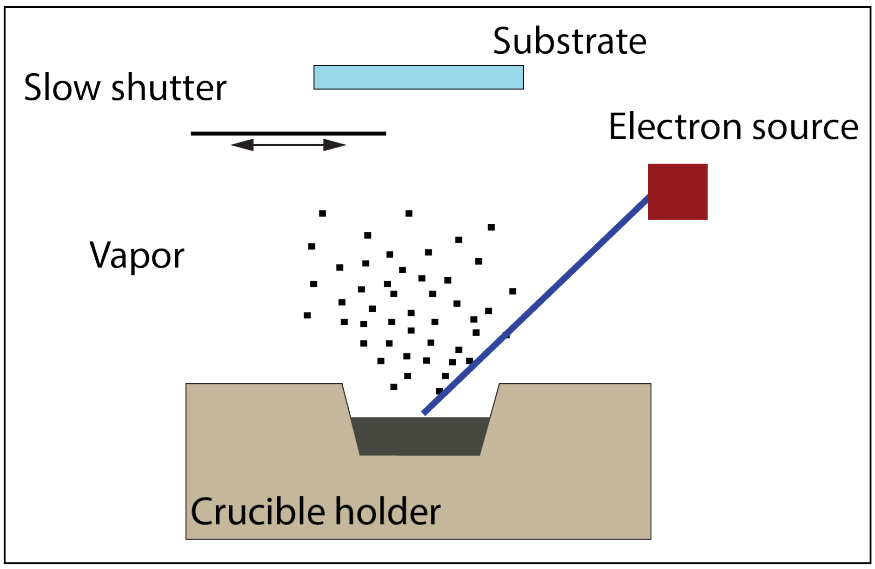

Figure 5.1: *Schematic representation of the e-beam physical vapor deposition (EB-PVD) thin film growth technique that was used to grow the TiO_x tapered waveguide. This technique uses an electron beam to heat up the precursor in the vacuum chamber, which vaporizes and spreads through the vacuum chamber. The vapor deposits onto the glass substrate that is placed above the crucible, which forms a thin film because of the low deposition rate of 1 Å/s. O_2 gas is flown into the vacuum chamber during deposition to create a homogeneous and near stoichiometric TiO_2 film. Finally, the thin film is tapered on one side of the substrate by moving a slow shutter parallel to the substrate away from it. This creates a time varying 'shadow' for the vapor, causing the deposited film to be tapered to 0 over the distance by which the slow shutter moved in front of the substrate during deposition.*

Two TiO_x tapered waveguides were fabricated, with total deposition times of 40.5 and 82 minutes respectively. Figure 5.2 shows an image of the first TiO_x sample, with the TiO_x thin film on the left (purple), the bare glass on the right (gray), and the tapered waveguide in the middle (colored lines). Both tapered waveguides were deposited on a 2 cm x 2 cm x 1 mm glass substrate. The first tapered waveguide was expected to be 200 nm thick, being tapered down over a distance of 2 mm. The second tapered waveguide was expected to be 450 nm thick, being tapered down over a distance of 0.9 mm.

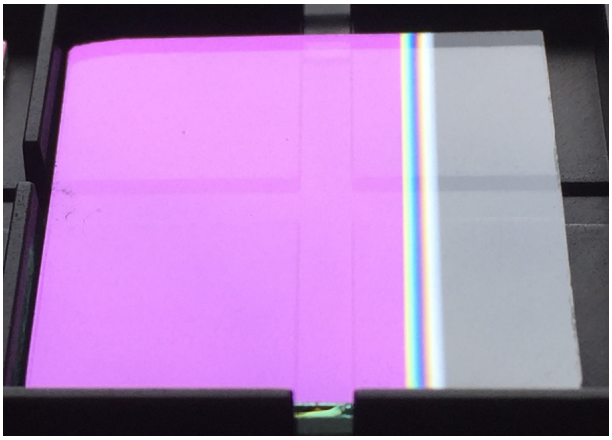

Figure 5.2: *Image of the first fabricated tapered waveguide, on a glass substrate (2 cm × 2 cm × 1 mm). The left part of the glass substrate is covered with a thin film of TiO_x (purple); the right part of the substrate is bare (gray). In between, a 2 mm wide tapered waveguide is visible from the colored lines, corresponding to the Fabry-Pérot resonances that change as a function of the film thickness.*

5.2 Tapered waveguide geometry analysis

The height profile of the tapered end of the second thin film was determined by profilometry, to ensure that the thin film is linearly tapered down. Figure 5.3 shows the profile scan, showing that the slope of the tapered waveguide is indeed linear (in between the dashed lines).

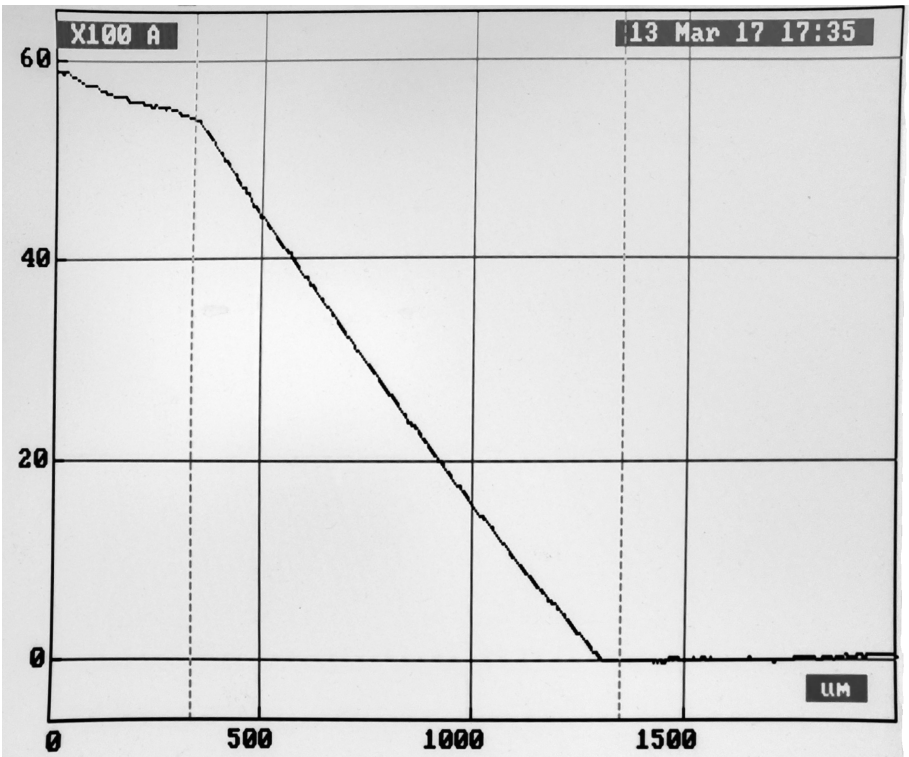

Figure 5.3: *Profilometry scan of the taper height as a function of its length, showing that the slope of the tapered waveguide is linear. In between the dashed lines, the film thickness increases linearly from 0 (glass substrate) to 5500 Å (uncalibrated value).*

The thickness calculation by profilometry is uncalibrated, so the final thickness of the samples is determined from reflection measurements that were performed on the TiO_x and the bare glass substrate. The substrate is expected to give a single-interface glass reflection, which is roughly 4% throughout the visible spectrum. In contrast, we expect multiple reflections within the TiO_x film to occur, causing Fabry-Pérot resonances to occur in the reflection spectrum. These resonances depend on the thickness of the thin film and on the wavelength, causing dips in the reflection spectrum when multiple reflections add up constructively inside the film. In general, constructive interference occurs for multiple reflections inside a thin film when we satisfy

$$2d\cos(\theta) = m\lambda, \tag{5.1}$$

with d the thickness of the film, θ the angle of the light path with respect to the normal, λ the wavelength of the light inside the material, and $m = 1, 2, 3, \ldots$ the order of the Fabry-Pérot resonance. Constructive interference implicates that less light is reflected back to the microscope objective, and causes a reflection drop for the wavelengths that satisfy eq. (5.1). To determine the thickness from such a measured spectrum, we can compare it to the theoretical reflection spectra for different thicknesses. The thickness, corresponding to the theoretical spectrum that matches the experimental spectrum best, is then the thickness of the fabricated thin film.

We calculate the theoretical reflection spectrum by starting from the Fresnel equations for reflection coefficients for TE and TM polarization (eqs. (4.34-35) and (4.40-41) in ref. [36, p. 114-115]),

$$r_{ij}^{TE} = \frac{n_i \cos(\theta_i) - n_j \cos(\theta_j)}{n_i \cos(\theta_i) + n_j \cos(\theta_j)}, \tag{5.2}$$

$$t_{ij}^{TE} = \frac{2n_i \cos(\theta_i)}{n_i \cos(\theta_i) + n_j \cos(\theta_j)}, \tag{5.3}$$

$$r_{ij}^{TM} = \frac{n_j \cos(\theta_i) - n_i \cos(\theta_j)}{n_j \cos(\theta_i) + n_i \cos(\theta_j)}, \tag{5.4}$$

$$t_{ij}^{TM} = \frac{2n_i \cos(\theta_i)}{n_j \cos(\theta_i) + n_i \cos(\theta_j)}, \tag{5.5}$$

where r_{ij} the reflection coefficient and t_{ij} the transmission coefficient for the interface between materials i and j, with refractive indices n_i and n_j respectively. Considering the 1 mm thick glass substrate to be infinitely thick compared to the focal depth of the confocal microscope ($\sim 1\mu m$), we can calculate the total reflection from the bare glass substrate by averaging the reflection coefficients for TE and TM modes (unpolarized light), and taking the absolute square. In contrast, for the thin TiO_x film, we need to consider multiple reflections within the thin film. Without deriving, we have the following expression for the reflection coefficient of a thin film (eq. (9.51) in ref. [36, p. 419]),

$$r_{film} = r_{12} + \frac{t_{12} r_{23} t_{21} \exp(i k_0 n_2 2 d_2 \cos(\theta_2))}{1 - r_{23} r_{21} \exp(i k_0 n_2 2 d_2 \cos(\theta_2))}, \tag{5.6}$$

where n_2 the refractive index of the TiO_x thin film and d_2 its thickness. Averaging this reflection coefficient for TE and TM polarization, we can take again the absolute square to obtain the reflection from the TiO_x thin film, as a function of its thickness d_2 and wave vector k_0. Comparing this calculated reflection spectrum to the measured reflection spectrum, we can find the thickness d_2 for which the calculated spectrum matches best with the measured spectrum. The reflection from the TiO_x thin film is measured using our WITec confocal microscopy system. In this confocal microscope, light focused on the TiO_x surface reflects and is collected by the objective (20x, $NA = 0.4$). The reflected light is sent to a spectrometer to determine the spectrum. This measured spectrum for the TiO_x thin film is normalized to percentages by relating it to the measured reflection spectrum for the bare glass substrate,

$$R_{TiO_x}(\%) = \frac{R_{m,TiO_x}}{R_{m,SiO_2}} \times R_{c,SiO_2}(\%), \tag{5.7}$$

with $R(\%)$ the reflection spectrum normalized to percentages, R_m the measured reflection spectrum and $R_c(\%)$ the calculated reflection from the Fresnel reflection coefficients. In addition to normalizing the measured spectrum to percentages, a normalization is performed to account for the power distribution over angles θ_1 (the incident angles from the confocal microscope objective). Figure 5.4 shows the calculated reflection spectra for the second TiO_x thin film on a glass substrate (green) and the bare glass substrate (blue), and the normalized reflection spectrum for the second fabricated TiO_x thin film on the glass substrate (red). The thickness for the calculated spectrum is set to $d_2 = 460$ nm, which shows good agreement with the normalized reflection spectrum in terms of the resonance minima. The difference between the maxima in the spectra is attributed to the roughness of the TiO_x film, which scatters part of the light away from the collection spot of the confocal microscope. The reflection spectrum for the first tapered waveguide is not shown but corresponds to a thickness of 246 nm.

For comparison, ellipsometry data was acquired for the second thin film to also determine the film thickness. This was done on a silicon slide, which was placed next to the glass substrate during the second TiO_x deposition, to obtain the same film thickness. The thickness determined by ellipsometry is 466 nm, proofing good agreement with the thickness determined from the reflection spectrum.

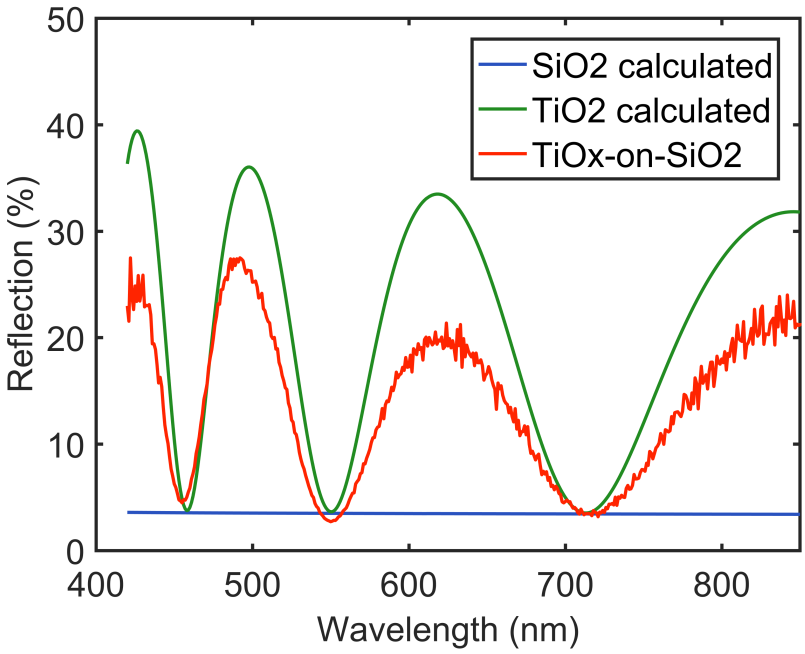

Figure 5.4: *Calculated and measured reflection from the TiO_x tapered waveguide as a function of wavelength. Using our WITec confocal microscopy system, we measure the reflection from both the TiO_x thin film and the bare glass substrate. Using equation eq.* (5.7)*, we calculate the reflection of the TiO_x film in percentages (red), showing characteristic Fabry-Pérot resonances in the visible. Comparing this to the calculated reflection for the TiO_x film (green), we find good agreement for the minima due to the resonances, but slightly lower maxima, which is attributed to roughness of the TiO_x film. A thickness of 460 nm was determined based on the Fabry-Pérot resonances.*

5.3 Scanning near-field optical microscopy setup

Following the proof of concept obtained by FDTD simulations of the TiO_2 tapered waveguide (see section 4.3.1), we designed an experiment to measure the spectrum-splitting behavior of the second fabricated taper (maximum height of 460 nm, length of 0.9 mm). FDTD simulations showed that the light radiates from the taper towards the substrate only, mainly between angles of 10-20° with respect to the horizontal. Because of this shallow angle, the light that radiates out of the taper will be confined to the glass substrate due to total internal reflection at the glass-air interface. Therefore, we cannot image the spectrum-splitting effect underneath the taper, as done in the FDTD simulation. However, using scanning near-field optical microscopy (SNOM), we can collect part of the evanescent field of the total internal reflected light at the glass-air interface. In this technique, a microscopic tip with a 100 nm aperture is brought in contact with the sample. Using a deflection laser, the position of the tip in the vertical direction is corrected for to ensure that the tip stays just in contact with the surface as it is scanned over it, similar to the functioning of an atomic force microscopy (AFM) tip. Because of the aperture in the SNOM tip, the evanescent field of the total internal reflected light is perturbed and is able to move through the aperture, where it is collected by the microscope objective.

Figure 5.5 shows a schematic representation of the designed experimental setup, using SNOM to measure the spectrally-split light. In this setup, a lensed fiber is positioned in front of the side of the TiO_x thin film, to couple in a white light source. The light travels through the waveguide and radiates into the substrate as it reaches the taper. At the glass-air interface, we measured the SNOM signal as a function of distance but did not obtain any signal. We optimized the setup by changing the manual micrometer manipulation stage to a piezo stage for better control over the position of the lensed fiber, to ensure stable and precise in-coupling of the laser light into the waveguide. Also, we ensured transmission through the SNOM tip was nonzero, and finally, we got rid of sample-holder reflections

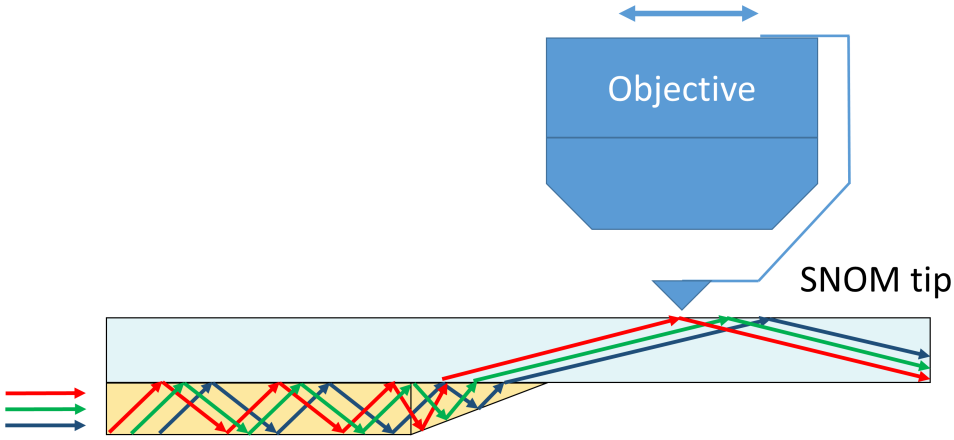

Figure 5.5: *Schematic representation of the side view of the experimental setup, employing SNOM to collect part of the total internal reflected light at the glass-air interface. A lensed fiber is positioned in front of the thin-film waveguide to couple a white light source into the waveguide. At the tapered end of the thin-film, light gets spectrally split and radiates out of the waveguide towards the glass side. By scanning the SNOM tip and objective horizontally, a scan of light spectra as a function of distance can be made, which is expected to show different colors at different positions, according to the spectrum-splitting capabilities of the tapered waveguide.*

entirely. This again led to zero signal, leading us to re-examine the expected radiation direction from the tapered waveguide. For the design of this experiment, the radiation angle from FDTD simulations of around 15° was taken as the expected radiation angle (see Figure 4.9). However, the length of the taper in the simulation and the length of the taper in the experiment are not the same (25 μm vs. 1 mm, respectively), while the thickness is the same. From the ray optics perspective, we can intuitively understand that this affects the power per radiation angle. Looking again at Figure 4.3, we see that upon each up- and down movement, the angle of incidence changes by 2α, whose value gets smaller as the tapered waveguide gets longer. That means that for a longer tapered waveguide, a light wave will hit the substrate interface more times per angle of incidence. That implicates that it refracts part of its energy under shallower angles more often than a short taper. So, the main radiation angle with respect to the horizontal scales inversely with the taper length.

For our experiment, this explains why we did not get any SNOM signal: the light radiates out under such a shallow angle for it to never hit the glass-air interface on the bottom, but rather on the side. Thus, it will not be possible to image the spectrum-splitting behavior on the rear-side of the glass substrate. Because of this (late) insight, we rethought our experimental setup and came up with two different setups that are expected to be able to measure spectrum-splitting under a very shallow angle, which are explained in the next section. Due to the time limit of this master project, these setups have not been build yet, but they will be built in the near future.

5.4 Redesigned experimental setups

The first redesigned experimental setup is very similar to the SNOM setup shown in Figure 5.5. However, we now place the microscope objective, on the side of the waveguide and image the light as a function of distance on the side of the glass substrate (see Figure 5.6). In contrast to the SNOM setup, the light will reach the glass-air interface on the side and refract at the interface because of the shallow angle with respect to the normal. Therefore, we can omit the SNOM tip and directly collect the light with the objective positioned on the side of the glass substrate. The objective should then be scanned in the vertical direction by a piezo stage to obtain a spectrum at each position. If this piezo stage has a resolution that is higher than the spatial distribution of the spectrally-split light, then the peak wavelength in the spectra is expected to redshift as the objective moves downwards.

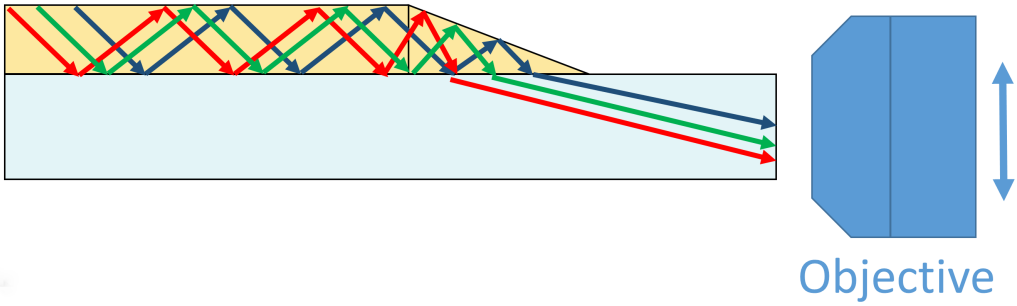

Figure 5.6: *Similar measurements setup to the initial SNOM setup shown in Figure 5.5. Instead of measuring the SNOM signal on the bottom of the glass substrate, we now image the radiation on the side of the substrate, directly with the microscope objective. By scanning the objective in the vertical direction with a piezo stage, we obtain spectra that are expected to change as a function of position, according to the spectrum-splitting behavior of the tapered waveguide.*

In addition to the setup proposed above, we propose another setup where the objective is replaced by a bare CCD chip, as shown in Figure 5.7. The CCD chip is able to detect the power as a function of distance, so we are not able to distinguish between wavelengths as with the objective and spectrometer used in the previous setups. Instead, we must use a single wavelength laser source and obtain the power at this wavelength as a function of distance. Then, we find the power distribution over the distance as a function of wavelength by sweeping the wavelength of the power source. In order to obtain a spatial power shift as a function of the source wavelength, the resolution of the CCD chip should be higher than the spatial distribution of the spectrally-split light. We thus need to determine this distribution, similar as for the previous setup.

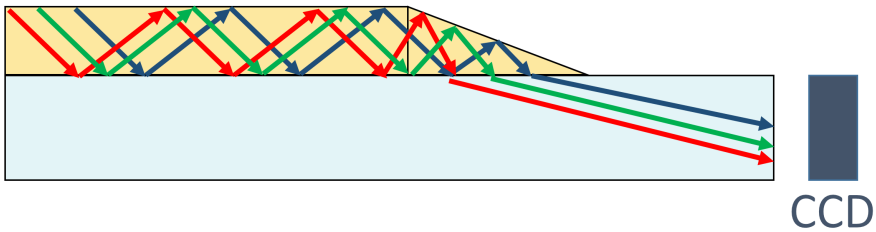

Figure 5.7: *Different measurements mechanism, as compared to the initial SNOM setup shown in Figure 5.5. By placing a CCD camera chip on the side the glass substrate, radiated power as a function of distance is recorded. By sweeping the wavelength of a single wavelength source, we could then map the wavelength as a function of distance, recovering the spectrum-splitting effect.*

Because in the proposed measurement setups the light is collected from the side facet of the glass substrate, we must ensure that this surface is smooth to prevent scattering. However, the glass substrates are cut from bigger wafers, but not smoothly polished. To determine the smoothness of the glass side surface, we took scanning electron microscopy (SEM) images of the side facet under a 45° angle. Figure 5.8 shows images of a smooth region of the glass side facet (a), a rough region of the glass side facet (b), and a zoom in of the TiO_x thin film side facet on the glass substrate (c). The roughness of both the glass and the TiO_x thin film side facets indicates that we need to polish these surfaces for future measurements, to ensure both efficient in-coupling into the TiO_x film and out-coupling from the glass side facet.

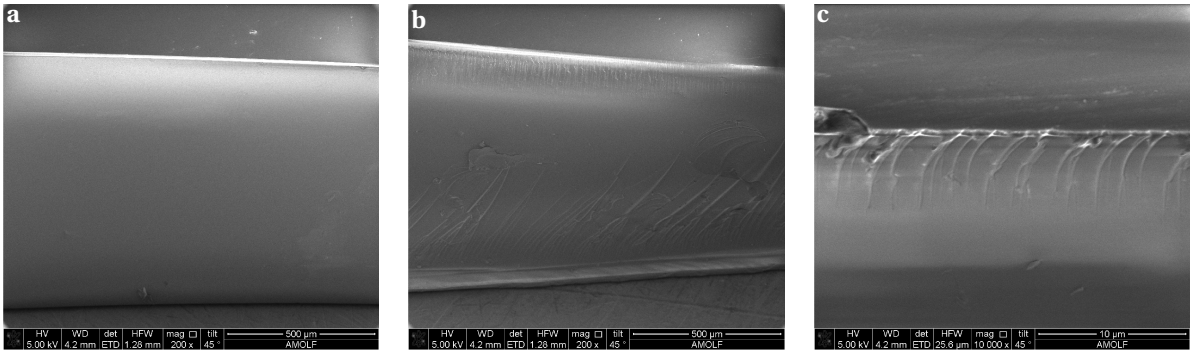

Figure 5.8: *SEM images of the side facet of the glass substrate (1 mm thick), with the TiO_x thin film on top (460 nm thick). (a) Smooth region of the glass side, for which polishing doesn't seem necessary. (b) Rough region of the glass side, for which polishing is certainly necessary. (c) Zoom in of the TiO_x thin film on top of the glass substrate, showing both the rough glass and the rough TiO_x side facets. Therefore, for future experiments, it is necessary to polish the in- and out-coupling sides of the tapered waveguide samples.*

5.5 Conclusion and outlook

In this chapter, we have described the successful fabrication of the TiO_x tapered waveguides. Subsequently, we have characterized the waveguides using reflection measurements, and compared those to the theoretical reflection spectra to determine the thickness from the Fabry-Pérot resonances. In addition, we showed the linear shape of the tapered waveguide from profilometry. To demonstrate the spectrum-splitting effect, we designed a measurement setup using SNOM to probe the spectrally-split light inside the glass substrate. However, due to incorrect expectations based on FDTD simulations of a shorter tapered waveguide, this setup was not able to measure the effect. Anticipating very shallow radiation angles for our millimeter sized tapered waveguides, we designed two experimental setups to image and quantify their spectrum-splitting behavior. Due to the time limit of this master project, these setups could not be build yet.

Future experimental work will start with building the redesigned experimental setups, to demonstrate the expected spectrum-splitting capabilities of our tapered waveguides. When we understand the spectrum-splitting behavior from experiments, we can return to theory and simulations to design more complex tapered waveguides. For instance, for integration of the tapered waveguide into a parallel-stacked tandem solar cell geometry, we might want to separate the spectral bands further apart. To achieve this, we could for instance design a tapered waveguide consisting of tapered regions, alternated with flat regions. Also, we could think of combining the inverse design algorithm optimization described in chapter 3 with the spectrum-splitting objective of the tapered waveguide to design the optimal shape of the taper. Finally, we will investigate what kind of in-coupling scheme can achieve high efficiencies regarding the collection of the solar spectrum in a thin film waveguide, as schematically shown in Figure 4.1. Combining such a scheme with the tapered waveguide, we can then start dreaming of the realization of a parallel-stacked tandem solar cell with integrated, waveguide-based spectrum-splitter.

References

[1] A. Polman and H. A. Atwater, *Photonic design principles for ultrahigh-efficiency photovoltaics*, Nature Materials **11**, 174 (2012).

[2] International Energy Agency IEA, *Solar Photovoltaic Energy*, Technology Roadmap , 60 (2014).

[3] W. Shockley and H. J. Queisser, *Detailed balance limit of efficiency of p-n junction solar cells*, Journal of Applied Physics **32**, 510 (1961).

[4] A. Polman, M. Knight, E. C. Garnett, B. Ehrler, and W. C. Sinke, *Photovoltaic materials - present efficiencies and future challenges*, Science **352**, 307 (2016).

[5] C. D. Bailie and M. D. McGehee, *High-efficiency tandem perovskite solar cells*, MRS Bulletin **40**, 681 (2015).

[6] S. P. Bremner, M. Y. Levy, and C. B. Honsberg, *Analysis of tandem solar cell efficiencies under AM1.5G spectrum using a rapid flux calculation method*, Progress in Photovoltaics: Research and Applications **16**, 225 (2008).

[7] M. A. Green, Y. Hishikawa, W. Warta, E. D. Dunlop, D. H. Levi, J. Hohl-Ebinger, and A. W. Y. Ho-Baillie, *Solar cell efficiency tables (version 50)*, in *Prog. Photovolt: Res. Appl.*, volume 25, pages 668–676, 2017.

[8] K. Tanabe, *A review of ultrahigh efficiency III-V semiconductor compound solar cells: Multijunction tandem, lower dimensional, photonic up/down conversion and plasmonic nanometallic structures*, Energies **2**, 504 (2009).

[9] S. H. Moon, S. J. Park, S. H. Kim, M. W. Lee, J. Han, J. Y. Kim, H. Kim, Y. J. Hwang, D.-K. Lee, and B. K. Min, *Monolithic DSSC/CIGS tandem solar cell fabricated by a solution process*, Scientific Reports **5**, 8970 (2015).

[10] J. Li, N. Verellen, D. Vercruysse, T. Bearda, L. Lagae, and P. Van Dorpe, *All-Dielectric Antenna Wavelength Router with Bidirectional Scattering of Visible Light*, Nano Letters **16**, 4396 (2016).

[11] Y. H. Fu, A. I. Kuznetsov, A. E. Miroshnichenko, Y. F. Yu, and B. Luk'yanchuk, *Directional visible light scattering by silicon nanoparticles.*, Nature Communications **4**, 1527 (2013).

[12] D. Vercruysse, Y. Sonnefraud, N. Verellen, F. B. Fuchs, G. Di Martino, L. Lagae, V. V. Moshchalkov, S. A. Maier, and P. Van Dorpe, *Unidirectional side scattering of light by a single-element nanoantenna*, Nano Letters **13**, 3843 (2013).

[13] S. Person, M. Jain, Z. Lapin, J. J. Sáenz, G. Wicks, and L. Novotny, *Demonstration of zero optical backscattering from single nanoparticles*, Nano Letters **13**, 1806 (2013).

[14] E. Rusak, I. Staude, M. Decker, J. Sautter, A. E. Miroshnichenko, D. A. Powell, D. N. Neshev, and Y. S. Kivshar, *Hybrid nanoantennas for directional emission enhancement*, Applied Physics Letters **105**, 0 (2014).

[15] G. Mie, *Beiträge zur Optik trüber Medien, speziell kolloidaler Metallösungen*, Annalen der Physik **330**, 377 (1908).

[16] N. Yu, P. Genevet, M. A. Kats, F. Aieta, J.-P. Tetienne, F. Capasso, and Z. Gaburro, *Light Propagation with Phase Discontinuities Reflection and Refraction*, Science **334**, 333 (2011).

[17] P. Wang, J. A. Dominguez-Caballero, D. J. Friedman, and R. Menon, *A new class of multi-bandgap high-efficiency photovoltaics enabled by broadband diffractive optics*, Progress in Photovoltaics: Research and Applications **23**, 1073 (2015).

[18] X. Ni, N. K. Emani, A. V. Kildishev, A. Boltasseva, and V. M. Shalaev, *Broadband Light Bending with Plasmonic Nanoantennas*, Science **335**, 427 (2012).

[19] A. Y. Piggott, J. Lu, K. G. Lagoudakis, J. Petykiewicz, T. M. Babinec, and J. Vučković, *Inverse design and demonstration of a compact and broadband on-chip wavelength demultiplexer*, Nature Photonics **9**, 374 (2015).

[20] M. L. Brongersma, Y. Cui, and S. Fan, *Light management for photovoltaics using high-index nanostructures.*, Nature materials **13**, 451 (2014).

[21] J. van de Groep, D. Gupta, M. A. Verschuuren, M. M. Wienk, R. A. J. Janssen, and A. Polman, *Large-area soft-imprinted nanowire networks as light trapping transparent conductors*, Scientific Reports **5**, 11414 (2015).

[22] C. Van Lare, G. Yin, A. Polman, and M. Schmid, *Light Coupling and Trapping in Ultrathin Cu(In,Ga)Se_2 Solar Cells Using Dielectric Scattering Patterns*, ACS Nano **9**, 9603 (2015).

[23] G. Yin, M. W. Knight, M. C. van Lare, M. M. Solá Garcia, A. Polman, and M. Schmid, *Optoelectronic Enhancement of Ultrathin $CuIn_{1-x}Ga_xSe_2$ Solar Cells by Nanophotonic Contacts*, Advanced Optical Materials **5** (2017).

[24] V. Neder, S. L. Luxembourg, and A. Polman, *Efficient colored silicon solar modules using integrated resonant dielectric nanoscatterers*, Applied Physics Letters (in press).

[25] J. Kennedy and R. Eberhart, *Particle swarm optimization*, 1995 IEEE International Conference on Neural Networks (ICNN 95) **4**, 1942 (1995).

[26] J. Lu and J. Vučković, *Inverse design of nanophotonic structures using complementary convex optimization.*, Optics express **18**, 3793 (2010).

[27] J. Lu and J. Vučković, *Objective-first design of high-efficiency, small-footprint couplers between arbitrary nanophotonic waveguide modes*, Optics Express **20**, 7221 (2012).

[28] J. Lu and J. Vučković, *Nanophotonic computational design*, Optics Express **21**, 13351 (2013).

[29] A. Y. Piggott, J. Lu, T. M. Babinec, K. G. Lagoudakis, J. Petykiewicz, and J. Vučković, *Inverse design and implementation of a wavelength demultiplexing grating coupler.*, Scientific reports **4**, 7210 (2014).

[30] A. Y. Piggott, J. Petykiewicz, L. Su, and J. Vučković, *Fabrication-constrained inverse design of a broadband 3-way power splitter*, page 1 (2016).

[31] D. A. B. Miller, *All linear optical devices are mode converters*, Optics Express **20**, 23985 (2012).

[32] `https://github.com/JesseLu/objective-first/`.

[33] P. K. Tien, *Light Waves in Thin Films and Integrated Optics*, Applied Optics **10**, 2395 (1971).

[34] M. Born and E. Wolf, *Principles of Optics: Electromagnitic theory of propagation, interference and diffraction of light*, Cambridge University Press, seventh edition, 1999.

[35] P. K. Tien and R. J. Martin, *Experiments on light waves in a thin tapered film and a new light-wave coupler*, Applied Physics Letters **18**, 398 (1971).

[36] E. Hecht, *Optics*, Addison Wesley, fourth edition, 2002.

Summary

Current commercially available solar cells are mostly single-junction (silicon) modules, which are inherently limited by the Shockley-Quiesser efficiency limit of 33.4 %. In the pursuit of cheap, sustainable solar energy harvesting, we propose a novel parallel-stacked multi-junction solar cell architecture. This architecture overcomes the limits and losses associated to conventional multi-junction solar cells while maintaining the higher Shockley-Quiesser efficiency limit, as described in the Introduction of this thesis. The key component of such a parallel-stacked tandem is a spectrum-splitting layer, which reroutes distinct spectral bands of the solar spectrum to the subcells with corresponding bandgaps. In this thesis, three different approaches to such a spectrum-splitting layer are investigated.

In Chapter 2, we investigate the use of a bidirectional scattering V-shaped nanoantenna as the building block of a spectrum-splitting metasurface. Based on earlier work by Li et al. [10], we reproduce the bidirectional scattering behavior in FDTD simulations. In addition to this earlier work, we normalize the extinction of the incident light by the geometrical cross section of the V-shaped antenna, therewith quantifying the extinction to be 8 times larger than the geometrical cross section around a wavelength of 700 nm. When designing a metasurface composed of antennas, it is important to know the influence that individual antennas have on each others behavior when they are placed in each other's near field. Therefore, we place two V-shaped antennas close together in FDTD simulations, and show that they maintain their bidirectional scattering behavior, even for very small distances between them. Moreover, the bidirectional scattering efficiency is ~1.5 times higher when two V-shaped antennas are placed very close together, relative to a single antenna. This result paves the way for the envisioned spectrum-splitting metasurface, based on bidirectional scattering V-shaped antennas.

In Chapter 3, we design 2D optimized visible light manipulating structures by using the inverse design algorithm, which was developed and proven successful for infrared wavelengths by the Vuĉković group at Stanford University [19, 26–30]. We first show that the initial electric permittivity defined in the optimization algorithm affects the final optimized design, which has not been reported so far. Then, we change the material properties to be transparent for the visible spectrum, which is needed for the purpose of efficient solar spectrum-splitting. The transparent optimized structure becomes less efficient but more robust to fabrication constraint than the non-transparent structure. This robustness may be an advantage of the transparent structure, if the efficiency can be increased by, for example, changing the optimization problem and/or input parameters. If this can be shown in future work, this paves the way for inverse designed, high-efficiency, visible light manipulation structures such as a solar spectrum-splitter.

In Chapters 4 and 5 we describe, respectively, the theoretical and experimental work on our tapered waveguide spectrum-splitting concept. This concept is based on an asymmetric thin-film waveguide that is tapered down to zero in height. Light in the tapered end of this waveguide radiates into the substrate as a function of wavelength and taper thickness, thereby separating the wavelengths that are present in the waveguide. Chapter 4 introduces the theoretical framework of the asymmetrical tapered waveguide and its spectrum-splitting properties. In addition, results from analytical calculations and numerical FDTD simulations are shown as a proof of concept of spectrum-splitting by a tapered waveguide. Subsequently, Chapter 5 reports the fabrication procedure of two TiO_x tapered waveguides on a glass substrate. The tapered waveguides are shown to have a linear slope and a controllable final thickness. Finally, we describe the scanning near-field optical microscopy (SNOM) setup we employed to experimentally probe the spectrum-splitting behavior of the

tapered waveguide inside the glass substrate. However, due to incorrect extrapolation of the results from FDTD simulations, this setup was not able to measure the effect. Therefore, two alternative experimental setups are described, based on the insights gained from the SNOM setup, that we will build in future work to demonstrate the spectrum-splitting behavior of the tapered waveguide.

Overall, this thesis provides insights in the manipulation of visible light by nanophotonic structures. These insights can be used for the design and optimization of spectrum-splitting devices for novel multi-junction solar cell architectures and other optoelectronic applications.

Acknowledgements

Although I finish my master's degree by means of this thesis, I could not have come this far without the wonderful people surrounding me. Therefore, I would like to thank all the people that contributed to the work performed in my master project.

Allereerst wil ik Albert Polman bedanken voor deze kans deel uit te mogen maken van de Photonic Materials group. Jouw enthousiasme en optimisme hebben mij vanaf de eerste kennismaking geïnspireerd. De manier waarop vragen stelt, en kansen en oplossingen ziet in het onderzoek heeft mij veel geleerd. Ik heb veel zin om de komende vier jaar als promovendus in jouw groep verder te gaan met onderzoek naar het splitsen van het zonnespectrum.

Next, I would like to thank Mark Knight, who was my daily supervisor during the first 6 months of my master project. You have thought me incredibly much in those 6 months, across many topics, ranging from Lumerical FDTD simulations to presenting, and from computer scripting to efficient research practices. Also outside of physics, I learned a ton, for instance about photography, English language, politics and squash. All this learning was often accompanied by jokes and gezelligheid, to which I think back with pleasure.

My experience of conducting research during the past 11 months would not have been the same without the company of the Photonic Materials research group. I've felt part of the group from day one and I'm grateful for all the support, talks and shared experiences, both research related and private. I'm proud to be part of this group and am looking forward to many interesting and fun years to come! Thank you Toon, Verena, Sophie, Magda, Andrea, Nick, Cyrian, Daniel and Joris.

All the members of the Center for Nanophotonics I would also like to thank, especially for their discussions and feedback during the weekly colloquia and poster sessions. Not only have you contributed to my research by commenting on the work I presented, but also have I learned very much from the work presented by you and the discussions about it. It's the effort of the whole department that makes the colloquia and poster sessions so fruitful and of such high quality. I look forward to being working with you in this unique learning environment.

Het experimentele deel van dit masteronderzoek had ik niet uit kunnen voeren zonder de hulp van de supportafdelingen van AMOLF. Ik ben er van overtuigd dat AMOLF zo succesvol is door de directe samenwerking met alle experts van de verschillende supportafdelingen. Hartelijk dank voor alle hulp. Voor mijn project wil ik met name Andries Lof bedanken: jouw expertise en uitleg over de electronenmicroscopen, ellipsometrie en de Kameleon opdampsysteem hebben de fabricage en karakterisering van mijn samples mogelijk gemaakt in korte tijd. Ook Dion Ursem wil ik speciaal bedanken: jouw hulp in het optische lab en snelle oplossingen voor de experimentele opstelling hebben er voor gezorgd dat we zo snel al spectrum-splitsing metingen konden uitvoeren.

All the people that I've named so far have helped me in various ways, and have also made me feel home at AMOLF. But its really the whole AMOLF community that creates the social and happy atmosphere I have always felt. The numerous coffee breaks, lunch breaks and (overtime) dinners with people from all different departments within AMOLF, but also the squash and soccer games, borrels, and personeelsverening and NWO events, have made my time at AMOLF very joyful and fun. I would like to thank each and every one of you for making AMOLF the community it is!

Ten slotte wil ik iedereen om mij heen bedanken buiten AMOLF. In het bijzonder mijn vader en moeder, broers en zusje, verdere familie en vrienden. Ik voel me ontzettend rijk met zo veel lieve mensen om me heen, die altijd achter mijn keuzes staan.

AMOLF

The work described in this thesis has been performed at AMOLF, Science Park 104, 1098 XG Amsterdam, The Netherlands.